NIEMANN-PICK TYPE A DISEASE

Adeno-associated viral vector serotype 9–based gene therapy for Niemann-Pick disease type A

Lluis Samaranch[1]*†, Azucena Pérez-Cañamás[2]*, Beatriz Soto-Huelin[2]*, Vivek Sudhakar[1],
Jerónimo Jurado-Arjona[2], Piotr Hadaczek[1], Jesús Ávila[2], John R. Bringas[1], Josefina Casas[3],
Haifeng Chen[4], Xingxuan He[5], Edward H. Schuchman[5], Seng H. Cheng[6], John Forsayeth[1],
Krystof S. Bankiewicz[1†‡], María Dolores Ledesma[2‡]

Niemann-Pick disease type A (NPD-A) is a lysosomal storage disorder characterized by neurodegeneration and early death. It is caused by loss-of-function mutations in the gene encoding for acid sphingomyelinase (ASM), which hydrolyzes sphingomyelin into ceramide. Here, we evaluated the safety of cerebellomedullary (CM) cistern injection of adeno-associated viral vector serotype 9 encoding human ASM (AAV9-hASM) in nonhuman primates (NHP). We also evaluated its therapeutic benefit in a mouse model of the disease (ASM-KO mice). We found that CM injection in NHP resulted in widespread transgene expression within brain and spinal cord cells without signs of toxicity. CM injection in the ASM-KO mouse model resulted in hASM expression in cerebrospinal fluid and in different brain areas without triggering an inflammatory response. In contrast, direct cerebellar injection of AAV9-hASM triggered immune response. We also identified a minimally effective therapeutic dose for CM injection of AAV9-hASM in mice. Two months after administration, the treatment prevented motor and memory impairment, sphingomyelin (SM) accumulation, lysosomal enlargement, and neuronal death in ASM-KO mice. ASM activity was also detected in plasma from AAV9-hASM CM-injected ASM-KO mice, along with reduced SM amount and decreased inflammation in the liver. Our results support CM injection for future AAV9-based clinical trials in NPD-A as well as other lysosomal storage brain disorders.

INTRODUCTION

Inactivating mutations in the gene encoding the enzyme acid sphingomyelinase (ASM) cause an infantile neurovisceral deficiency of ASM named Niemann-Pick disease type A (NPD-A). A milder form of the disease, NPD-B, results in systemic organ pathology that includes hepatosplenomegaly and pulmonary dysfunction but no neurological deficits. In contrast, patients with NPD-A develop rapidly progressive mental deterioration with prominent loss of early motor skills and cognitive decline in addition to the systemic dysfunction of NPD-B (1, 2). Most patients with NPD-A are diagnosed after the appearance of symptoms at 3 to 6 months of age. A rapid neurodegenerative course leads to death before 3 years of age (3). Studies performed in a knockout mouse model lacking ASM gene (ASM-KO) and in cells derived from patients with NPD-A have demonstrated that abnormal accumulation of sphingomyelin (SM) and its lipid metabolites is the principal pathological event that leads to alterations in gene transcription (4), trafficking and distribution of various molecules (5), autophagy (6), synaptic function (7, 8), and calcium homeostasis (9). The ASM-KO mouse model develops ataxia and memory impairment, and has a reduced life span (8, 10). ASM is synthesized in the endoplasmic reticulum and is N-glycosylated in the Golgi (11). Its six oligosaccharide side chains

orchestrate the transport of the enzyme to lysosomes. However, a subset of enzyme undergoes processing into endoglycosidase-H–resistant molecules, which are then diverted into the secretory pathway, such as plasma membrane (12) and extracellular space (13). There is also constant recycling of lysosomal ASM to the cell surface. Recombinant human ASM (rhASM) (14) displays affinity for mannose-6-phosphate receptors and is rapidly taken up from the circulation of ASM-KO mice, primarily into the liver and spleen, where it is directed to acidified organelles and can degrade SM (15). This finding strongly suggested that enzyme replacement therapy (ERT) by intravenous infusion of rhASM would be a suitable strategy for the treatment of the peripheral symptoms in patients with NPD-A or NPD-B. A recent open-label phase 1b clinical trial (NCT0041566) has confirmed the safety of the ERT strategy and its potential efficacy to treat the non-neurological pathology in patients with ASM deficiency (16). A phase 2 clinical trial is currently ongoing for patients with NPD-B (NCT02004704) to evaluate long-term treatment with the recombinant enzyme. However, the absence of improvement in the neurological component after ERT in ASM-KO mice (15) suggested that this approach would be inadequate for patients with NPD-A. The differences between NPD-A and NPD-B progression are most probably due to the extremely low residual enzyme activity (less than 5% of normal activity) in tissues of patients with NPD-A compared to that in patients with NPD-B (17). Direct delivery of the rhASM into the lateral ventricles of ASM-KO mice elicited a broader distribution of the protein than the parenchymal injection and partially ameliorated the pathologic phenotype (18). However, when this approach was evaluated in nonhuman primates (NHP), lateral ventricle injection of rhASM resulted in very poor diffusion into the parenchyma and retention in the more superficial cortical layers even after repeated injections (19).

Replacement of the defective gene has been proven in preclinical and clinical research as a suitable therapy for a number of monogenic

[1]Department of Neurological Surgery, University of California San Francisco, San Francisco, CA 94103, USA. [2]Centro Biologia Molecular Severo Ochoa (CSIC-UAM), 28049 Madrid, Spain. [3]RUBAM, IQAC-CSIC & CIBEREHD, 08034 Barcelona, Spain. [4]Virovek Inc., Hayward, CA 94545, USA. [5]Department of Genetics and Genomic Sciences, Icahn School of Medicine at Mount Sinai, New York, NY 10029, USA. [6]Rare Disease, Sanofi, Framingham, MA 01701, USA.
*These authors contributed equally to this work.
†Present address: Department of Neurological Surgery, The Ohio State University, Columbus, OH 43210, USA.
‡Corresponding author. Email: dledesma@cbm.csic.es (M.D.L.); krzysztof.bankiewicz@osumc.edu (K.S.B.)

central nervous system (CNS) diseases (20), including certain lysosomal storage disorders (LSD). Hematopoietic stem cell gene therapy, in which ASM-KO bone marrow cells transduced with a retroviral vector encoding hASM were transplanted into ASM-KO mice, led to marked visceral improvement, but neurological abnormalities were only delayed (21). Direct brain injection of different serotypes of adeno-associated viral vector (AAV) carrying a competent copy of the human ASM gene has also been tested in ASM-KO mice (22–25). Common to all of these previous studies is the fact that viral vector injections reduced the presence of distended lysosomes and ameliorated the accumulation of cholesterol and SM. However, these improvements were limited to the injection site and immediate surrounding areas.

Various surgical approaches have been tested in NHP to improve vector distribution and to assess safety and feasibility. Infusion of rhASM into the lateral ventricle (19) resulted in reduced cortical distribution and no subcortical transduction due to a limited parenchymal permeation of the naked protein. Multiple parenchymal injections of AAV serotype 1 (AAV1)–hASM resulted in cortical and subcortical deposits (26), but despite the fact that total ASM expression in targeted areas increased, the lack of increase in distal areas suggested that additional injections to achieve clinically relevant widespread expression would be required. AAV2-hASM was infused by magnetic resonance (MR)–guided convection-enhanced delivery into the thalamus and brainstem (27, 28). However, a robust inflammatory response associated with weight loss and motor deficits was observed in high-dose NHP, defining dose-dependent toxicity (27). To facilitate vector distribution and to reduce highly focal expression, we have recently developed a cerebrospinal fluid (CSF) delivery method through the cerebellomedullary (CM) cistern that directs widespread transgene expression within the central and peripheral nervous systems in NHP (29). Also, we and others showed that AAV9 serotype efficiently transduces both neurons and glial cells either after systemic delivery (30, 31) or injection into the CSF (29, 32, 33). In the present study, we demonstrate the safety and dose-response efficacy of CM delivery of a recombinant AAV9 vector encoding hASM as a suitable therapeutic approach for severe ASM deficiency and provide a rationale for future AAV9-based clinical trials in NPD-A and other monogenic neurodegenerative diseases.

RESULTS

CM injection of AAV9-hASM in NHP elicits widespread brain expression of hASM without signs of toxicity

Previous experiments in NHP demonstrated that focal AAV2-mediated overexpression of high amount of hASM into the brain caused lymphocytic infiltration and ataxia (27). Here, 6 ml of AAV9-hASM at 2.3×10^{13} VG/ml was injected into the NHP CM to determine the safety of global hASM expression in the brain. After CM injection, animals showed no signs of toxicity such as weight loss, emesis, skin alterations, or behavioral abnormalities throughout in-life assessment up to 3 months after injection (table S1). Immunohistochemical staining (IHC) analysis of representative rostral-caudal sections 1 and 3 months after AAV9-hASM injection showed extensive cellular transduction, suggesting an intracellular lysosomal/endosomal distribution pattern of ASM protein in both cortical and Purkinje neurons of the AAV9-hASM CM-injected animals (Fig. 1, A and B) compared to the control (Fig. 1C). High-resolution confocal imaging of the immunofluorescently stained sections confirmed the pattern by showing colocalization of hASM with the

lysosomal marker LAMP-1 after treatment (Fig. 1D). Confocal imaging also evinced reduced lysosomal/endosomal signal at the 3-month survival time compared to the 1-month survival animals, supporting the impression of reduced accumulation of the protein over time due to a secretion process (fig. S1).

Quantitative analysis by infrared technology, a more sensitive method than diaminobenzidine-based IHC, showed that ASM-dependent infrared signal increased 1 month after AAV9-hASM CM injection in cortical areas, including hippocampus, and cerebellum compared to the control (Fig. 1E). Subcortical areas such as the thalamus also showed increased hASM expression (Fig. 1F). Quantitative analysis showed that after 3 months, ASM expression decreased in many areas, suggesting an active process of protein secretion (Fig. 1, E and F).

Other organs highly involved in the etiopathology of NPD-A, such as the liver and spinal cord, were also assessed to determine ASM expression by enzyme-linked immunosorbent assay (ELISA). Protein analysis showed expression of ASM in the liver and representative regions of the spinal cord (cervical, thoracic, and lumbar) (Fig. 1, G and H, respectively) compared to controls 1 month after injection. Spinal cord ASM expression remained high 3 months after injection especially in the lumbar region, suggesting accumulation of vector in that region after CSF delivery (33).

Determining whether AAV9-hASM CM injection triggered an immune response was an important goal of the experiments in NHP. Hematoxylin and eosin (H&E) staining showed no lymphocytic infiltration or luminal pathology in the blood vessels of any of the AAV9-hASM CM-injected animals at any time point (Fig. 1I). The absence of an immune reaction was confirmed by immunostaining for lymphocytic markers such as MHC-II (major histocompatibility complex II), CD4, CD8, and CD68 (fig. S2). All markers were negative in contrast to the staining observed in the historical tissue of NHP injected with AAV9–green fluorescent protein, which induced a strong immune response (32) and, therefore, was used as a positive control (fig. S2). Astrocytes and microglia were also evaluated by the specific markers glial fibrillary acidic protein (GFAP) and Iba1 to assess gliosis (fig. S2). GFAP-stained sections did not show any cortical astrocytic activation (fig. S2A) or signs of activated velate astrocytes in the granular layer or reactive Bergmann glial cells in the cerebellum (fig. S2B). Sections stained with anti-Iba1 antibodies indicated no hyperreactive microglial cells at any time point after AAV9-hASM injection, further confirming the absence of an immune response (fig. S2). Because previous studies with parenchymal infusions of AAV encoding hASM showed motor impairment, evidence of damage to Purkinje cells in cerebellum, along with reduction in calbindin amount after transgene overexpression (32), we analyzed the integrity of these cells by anti-calbindin staining. No loss of calbindin was seen in the AAV9-hASM CM-injected animals compared to control at any time point (37 ± 7, 37 ± 5, and 39 ± 15 calbindin-positive cells per frame in control NHP and in 1- and 3-month AAV9-hASM CM-injected NHP, respectively; $P = 0.954$) (Fig. 1J). To determine humoral immune response, circulating anti-AAV9 neutralizing antibodies [immunoglobulin G (IgG)] in the CSF and serum of the AAV9-hASM CM-injected NHP were titered by ELISA (29) at 1 and 3 months. Titer analysis showed that after injection, anti-capsid antibodies dilution slightly increase over time in sera (1:400 and 1:800, respectively) and in CSF (1:100 and 1:200, respectively), although animals remained seronegative according to the criteria used in clinical trials because their titers were lower than 1:1200 (34).

Fig. 1. CM injection of AAV9-hASM elicits broad transgene distribution in NHP brain and spinal cord with no neurological adverse effects or signs of histopathology. (**A** and **B**) Representative images of ASM protein expression in the cortex and cerebellum of NHP after CM delivery of 6 ml of 2.3×10^{13} VG/ml AAV9-hASM throughout CM injection at 1-month (A) and 3-month (B) survival time ($n = 1$ animal per group). Insets depict the intracellular lysosomal/endosomal distribution pattern of the hASM protein in the cells indicated by black arrowheads. (**C**) ASM protein expression in the cortex and cerebellum of control NHP not injected with AAV9-hASM. (**D**) Immunofluorescent colocalization of ASM and the lysosomal marker Lamp1 in Purkinje cells of the cerebellum. (**E**) Graphs showing the mean ± SEM of ASM-associated infrared signal per area in the indicated brain regions of noninjected NHP (white bars), 1-month survival NHP (black bars), and 3-month survival NHP (gray bars) after CM AAV9-hASM injection ($n = 1$ animal per group). (**F**) Graph showing mean ± SEM ASM-associated infrared signal per area in the thalamus of noninjected NHP (white bar), 1-month survival NHP (black bar), and 3-month survival NHP (gray bar) after CM AAV9-hASM injection ($n = 1$ animal per group). (**G**) Graph showing ASM amount in liver homogenates determined by ELISA in noninjected NHP (white bar), 1-month survival NHP (black bar), and 3-month survival NHP (gray bar) after CM AAV9-hASM injection ($n = 1$ animal per group). (**H**) Graphs showing ASM amount determined by ELISA in representative regions (cervical, thoracic, and lumbar) of the spinal cord of noninjected NHP (white bars) or in NHP 1 month (black bars) and NHP 3 months (gray bars) after CM AAV9-hASM injection ($n = 1$ animal

per group). (**I**) Representative images of H&E staining in cortex and cerebellum of NHP after CM delivery of AAV9-hASM throughout CM injection at 1- and 3-month survival time and in a noninjected control NHP. (**J**) Representative images of Purkinje cells within the cerebellum stained against calbindin in NHP after CM delivery of AAV9-hASM at 1- and 3-month survival time and in a noninjected control NHP. Scale bars, 50 μm for (A), (B), and (C) insets; 500 μm for (A) and (B) (top left); 200 μm for (A) and (B) (bottom left and top right), (C), (I), and (J); 100 μm for (A) and (B) (bottom right); 10 μm for (D). N, nucleus; a.u., arbitrary units. In (H), the symbol ⌘ in the control animal denotes levels of ASM lower than the detection limit of the ELISA kit. Statistical analyses were performed using two-way ANOVA followed by Tukey's post hoc test for multiple comparisons correction. *$P < 0.05$, **$P < 0.01$, and ***$P < 0.001$. N/A, not available.
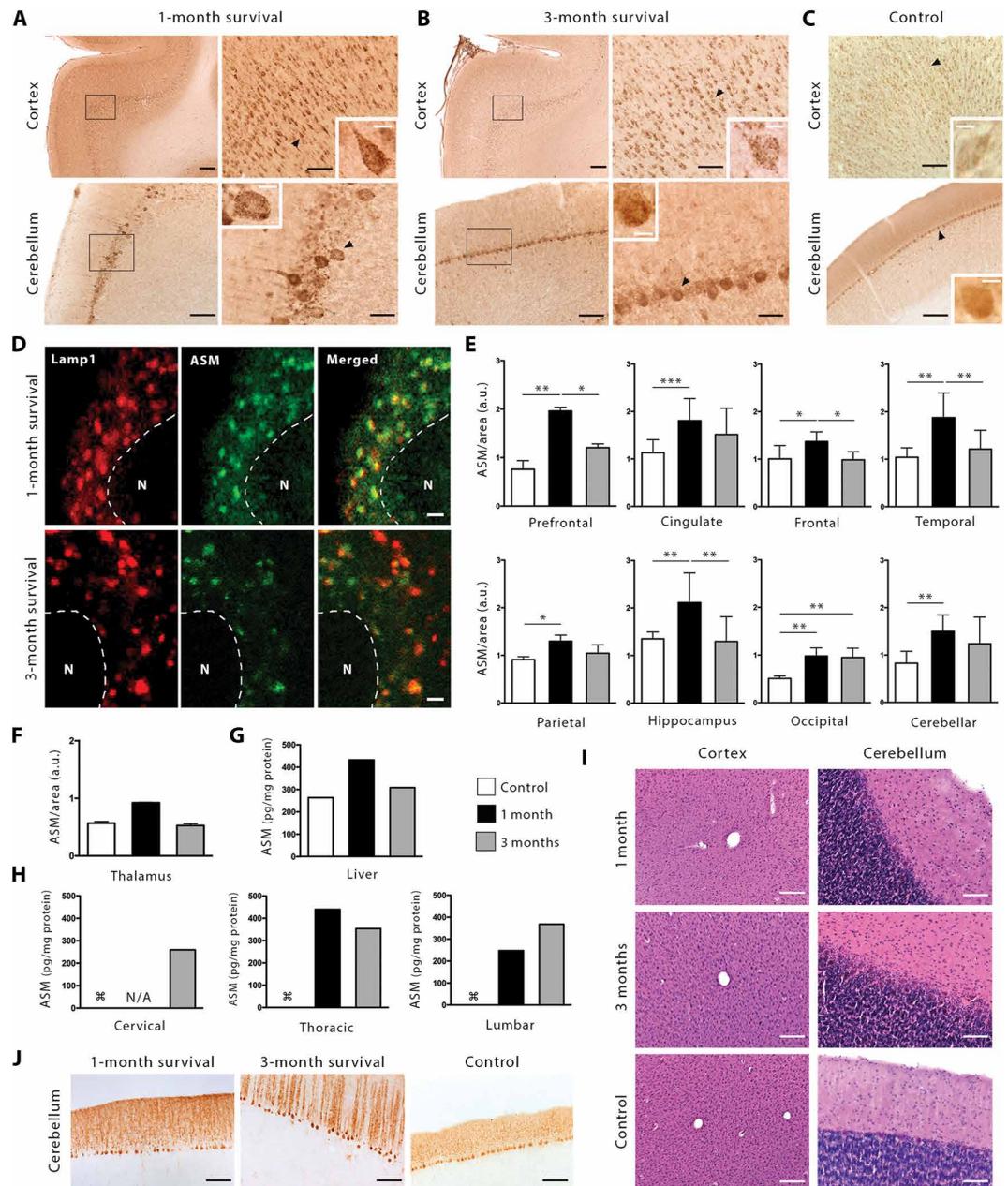
CM injection of AAV9-hASM in ASM-KO mice is dose-dependently efficacious

To evaluate vector efficacy, we performed a dose-response study in ASM-KO mice, a validated animal model for NPD-A that mimics the human disease (*10*, *35*). Wild-type (WT) and ASM-KO mice received CM injections of 10 μl of AAV9-hASM at three different concentrations (2.3×10^9, 2.3×10^{11}, or 2.3×10^{13} VG/ml) prepared as in the NHP experiments. WT and ASM-KO control mouse groups

were injected with equal volumes of artificial CSF (aCSF). Injections were performed at 7 weeks of age when accumulation of SM has already occurred in the brains of ASM-KO mice (*9*). Moreover, Purkinje cell death and vacancies, consistent with a wave of active neuronal degeneration, are evident at this stage in the cerebellum in ASM-KO mice, especially in the anterior lobes (*36*). Motor deficits are already present at this stage (*36*). Effects of vector injections were monitored for 2 months. During this period, body weight was

Samaranch *et al.*, *Sci. Transl. Med.* **11**, eaat3738 (2019)   21 August 2019

3 of 15

assessed weekly. No differences in weight gain were found between the groups (Fig. 2A). Immediately before terminating the in-life portion of the study, we assessed motor function as a read-out for the efficacy of the treatment (Fig. 2B). The rotarod performance test confirmed motor deficits in aCSF-injected ASM-KO mice compared to WT. AAV9-hASM–injected ASM-KO mice showed a higher latency to fall from the rod compared to aCSF-injected ASM-KO mice at the highest dose of vector (2.3×10^{13} VG/ml), yielding motor performance comparable to WT mice (Fig. 2B). AAV9-hASM injection in WT mice did not have any effect on motor abilities (Fig. 2B). To establish a read-out for the therapeutic dose, we measured ASM activity in the CSF of mice injected with 10 μl of 2.3×10^{13} VG/ml AAV9-hASM. ASM activity was not detectable in ASM-KO mice injected with aCSF but increased to 0.8 nmol ml^{-1} hour^{-1} in the CSF of the ASM-KO mice injected with AAV9-hASM. However, ASM activity was still lower compared to WT mice injected with aCSF (1.78 nmol ml^{-1} hour^{-1}). AAV9-hASM injection in WT animals resulted in a further increase in ASM activity to 4.25 nmol ml^{-1} hour^{-1} (Fig. 2C).

CM injection of AAV9-hASM in ASM-KO mice prevents cerebellar pathology as efficiently as cerebellar injection but without promoting inflammation

Because the earliest and more pronounced symptoms of pathology in the ASM-KO mice occur in the cerebellum (36), we compared the effects of the established therapeutic dose in this brain area when administered through CM injection or through intracerebellar (iCb) injection in ASM-KO mice. Age at injection and time allowed for transgene expression were the same for the two groups (7 weeks and 2 months, respectively). No differences in weight gain were observed during the 2-month expression period after iCb or CM injections (Fig. 2D). The rotarod performance test indicated improvement in ASM-KO mice injected by either approach compared to the aCSF-injected ASM-KO mice (Fig. 2E). No differences in latency were found between AAV9-hASM and aCSF CM-injected WT mice (Fig. 2E). We then analyzed hASM expression in the cerebellum with respect to cellular and molecular hallmarks of the disease. Injection of AAV9-hASM into cerebellum (iCb) directed hASM expression in numerous Purkinje cells (Fig. 3A). CM injection also promoted hASM expression in Purkinje cells, but fewer cells were transduced (Fig. 3A and fig. S3). Analysis of hASM expression in Purkinje cells of the anterior (lobes I to V), mid (lobes VI to VIII), and posterior (lobes IX to X) cerebellar lobes revealed no lobe-dependent differences in the number of hASM-expressing cells in the iCb- or CM-injected mice (fig. S3). Expression of hASM was observed not only in neurons but also in astrocytes and microglia in both iCb- and CM-injected mice (Fig. 3B). Quantification of hASM in cerebellar extracts by Western blot showed that hASM expression in the ASM-KO mice that received a CM injection was 12-fold lower than that in the iCb-injected mice (Fig. 3C).

To determine the extent to which hASM expression had an impact on SM degradation, we measured the concentration of this lipid in cerebellar tissue biochemically (5). ASM-KO mice injected with aCSF showed a twofold increase in SM amount compared to aCSF-injected WT mice (Fig. 3D). Injection of AAV9-hASM, either iCb or CM, diminished SM amount in cerebellar extracts of ASM-KO mice by 1.2- and 1.3-fold, respectively. No changes were observed in WT mice (Fig. 3D). Lysosome enlargement caused by the accumulation of SM, particularly in Purkinje cells, is considered a pathological

hallmark of ASM-KO cells (1, 36). We, therefore, measured lysosomal size in the Purkinje cell layer of the cerebellar cortex by immunofluorescence with an antibody against the lysosomal membrane protein, Lamp1. We observed enlargement of lysosomes in aCSF-injected ASM-KO mice compared to aCSF-injected WT mice (Fig. 3E). Consistent with the reduction in SM amount, lysosomes were smaller in the ASM-KO mice that received an iCb or CM injection of AAV9-hASM (46 and 30% size reduction, respectively). AAV9-hASM injection did not affect lysosomal size in WT mice. Purkinje cell loss in the cerebellum is another disease hallmark that accounts for motor deficits in ASM-KO mice. Therefore, we analyzed cell density in the cerebellum by anti-calbindin antibody immunofluorescence, and a drastic reduction in Purkinje cell number was observed in aCSF-injected ASM-KO compared to aCSF-injected WT mice (Fig. 3F). Purkinje cell death was particularly evident in the anterior lobe (fig. S4). This, together with the similar number of hASM-expressing cells in all lobes (fig. S3), suggests that AAV9-hASM infection is higher in the anterior lobe. Because down-regulation of calbindin staining could have occurred in unhealthy Purkinje cells, we also quantified cell loss by Nissl staining (fig. S4, C and D). This analysis confirmed the anterior lobe as the most affected by the disease. Both iCb and CM injections of AAV9-hASM prevented Purkinje cell loss to a similar extent [2.7- and 2.4-fold average-all lobes increase in Purkinje cell number, respectively, by calbindin staining (Fig. 3F), and 2.2- and 2-fold average-all lobes increase by Nissl staining]. iCb injection prompted Purkinje cell death (1.6-fold decrease in Purkinje cell number) in WT mice (Fig. 3F), particularly in the anterior lobe (fig. S4). This effect was not observed after CM injection (Fig. 3F and fig. S4) and could explain the motor deficits observed in the WT mice that received an iCb injection of AAV9-hASM (Fig. 2E).

A main goal of CM injection was to minimize surgical impact and the potential for local inflammatory response associated with a direct brain injection. Therefore, we analyzed brain inflammatory cells, astrocytes, and microglia, with antibodies against the respective cell markers, GFAP and Iba1. Increased intensity of the astrocytic marker and increased number of microglia showing amoeboid morphology were observed in the cerebellum of aCSF-injected ASM-KO compared to WT mice (Fig. 4). This is consistent with a basal inflammatory state in the disease. iCb injection of AAV9-hASM promoted a further increase in astrocytic marker intensity and number of non-amoeboid microglia in both WT and ASM-KO mice, which affected particularly the anterior and mid lobes (Fig. 4, A and B, and fig. S5, A and B). This increase was not observed in the ASM-KO or WT mice that received a CM injection of AAV9-hASM (Fig. 4, A and B, and fig. S5, A and B). Although amoeboid microglia persisted in the cerebellum of AAV9-hASM CM-injected mice, the area of these cells was reduced in all lobes (fig. S5C). Because inflammation might be a consequence of increased amount of proinflammatory SM metabolites, we compared the concentration of sphingosine, sphingosine-1-P, and ceramide in the cerebellum of AAV9-hASM iCb- and CM-injected ASM-KO mice. Mass spectrometry indicated that, although sphingosine and sphingosine-1-P concentration was similar (sphingosine in nanomoles per milligram of protein: 47 ± 8 aCSF iCb, 38 ± 3 AAV9-hASM iCb, and 43 ± 8 AAV9-hASM CM; sphingosine-1-P in picomoles per milligram of protein: 22 ± 8 aCSF iCb, 19 ± 1 AAV9-hASM iCb, and 20 ± 0.3 AAV9-hASM CM), ceramide concentration was 1.8-fold higher in the iCb-injected ASM-KO mice compared to the CM-injected ASM-KO mice (ceramide in nanomoles per milligram of protein: 2492 ± 116

Fig. 2. CM injection of a therapeutic dose of AAV9-hASM in ASM-KO mice results in motor improvement similar to iCb injection. (**A**) Mean ± SEM body weight gain in percentage respect to baseline (before treatment) in WT and ASM-KO mice during the 8 weeks after CM injection of 10 μl of aCSF or of AAV9-hASM at different concentrations (2.3×10^9, 2.3×10^{11}, and 2.3×10^{13} VG/ml). (**B**) Mean ± SEM time spent on the rod in the rotarod performance test in WT and ASM-KO mice CM injected with aCSF or AAV9-hASM at the different doses ($n = 4$ to 9 animals per group). Two-way ANOVA followed by Bonferroni post hoc. (**C**) Mean ± SEM ASM activity in the CSF of WT and ASM-KO mice 8 weeks after receiving 10 μl of aCSF or of AAV9-hASM (2.3×10^{13} VG/ml) by CM injection ($n = 3$ to 4 animals per group). Two-way ANOVA followed by LSD post hoc. (**D**) Mean ± SEM body weight gain in percentage with respect to baseline (before treatment) in WT and ASM-KO mice during 8 weeks after iCb (left) or CM (right) injection of 10 μl of aCSF or of AAV9-hASM (2.3×10^{13} VG/ml). (**E**) Mean ± SEM time spent on the rod in the rotarod performance test in WT and ASM-KO mice after iCb or CM injection of 10 μl of aCSF or of AAV9-hASM (2.3×10^{13} VG/ml) ($n = 4$ to 7 animals per group). Two-way ANOVA followed by Games-Howell (iCb) and Bonferroni (CM) post hoc; *$P < 0.05$, **$P < 0.005$, and ***$P < 0.001$. n.s., not significant.
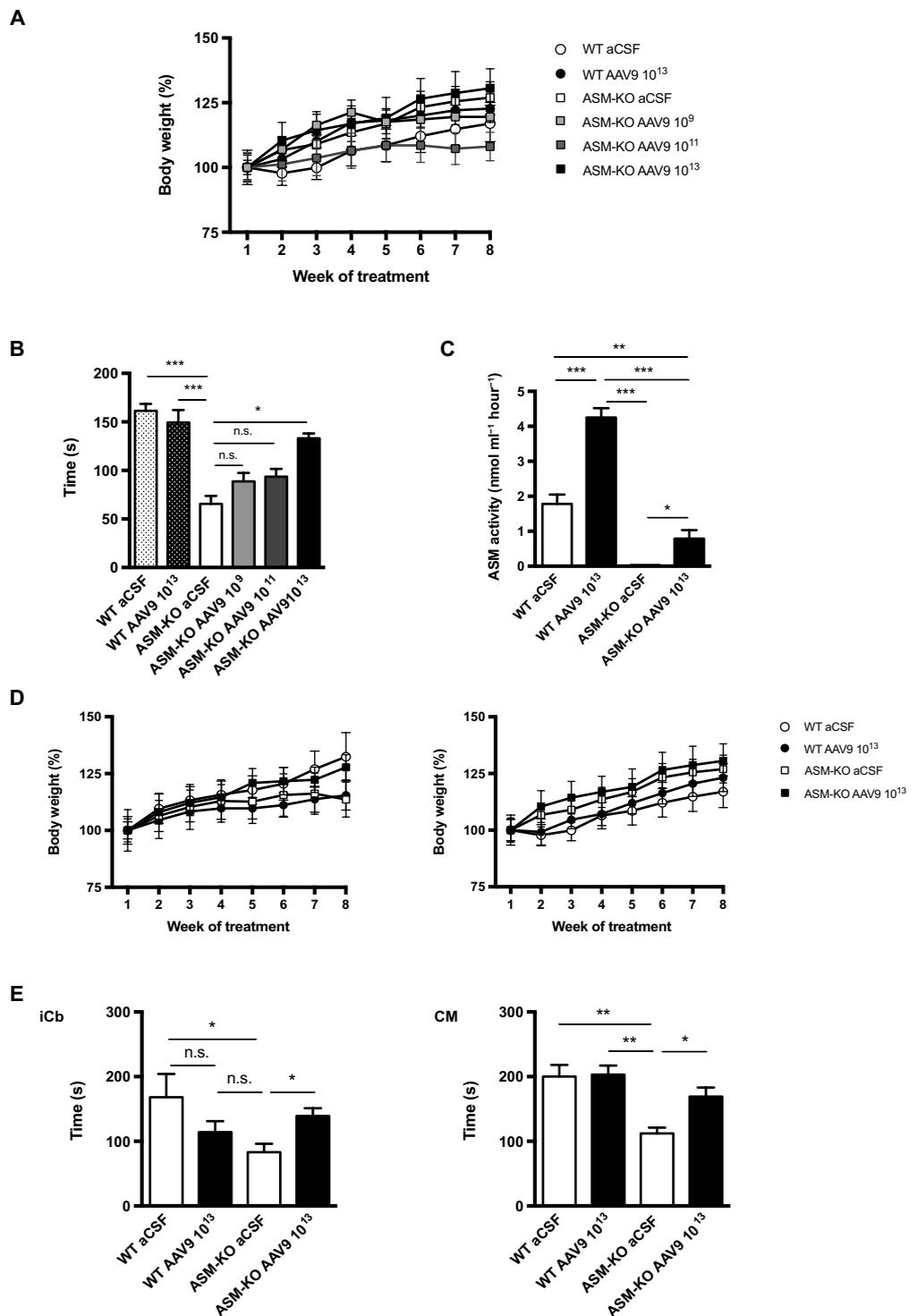

aCSF iCb, 3246 ± 178 AAV9-hASM iCb, and 1791 ± 124 AAV9-hASM CM). Although less pronounced than in the AAV9-hASM iCb, ASM-KO-injected mice showed a 1.16-fold increase in ceramide after AAV9-hASM treatment compared to aCSF iCb-injected WT mice (ceramide in nanomoles per milligram of protein: 1509 ± 47 aCSF iCb and 1762 ± 170 AAV9-hASM iCb), whereas sphingosine and sphingosine-1-P content showed no differences (sphingosine in nanomoles per milligram of protein: 45 ± 4 aCSF iCb and 32 ± 3 AAV9-hASM iCb; sphingosine-1-P in picomoles per milligram of protein: 69 ± 6 aCSF iCb and 58 ± 7 AAV9-hASM iCb) (fig. S6). This last result may help explain the inflammation (Fig. 4, A and B) and Purkinje cell death (Fig. 3F) detected in the AAV9-hASM iCb-injected WT mice.

Additional negative controls for the AAV9-hASM CM injection compared all the above read-outs with naïve noninjected and empty AAV9 vector CM-injected ASM-KO mice. No differences were found between naïve noninjected ASM-KO mice and ASM-KO mice CM-injected with the empty vector in motor and memory abilities and cerebellar SM content, lysosomal size, gliosis, and Purkinje cell survival. Both groups showed similar results to the aCSF CM-injected ASM-KO mice (fig. S7).

Together, these results show that CM injection of AAV9-hASM promoted a safer expression of hASM in glia and neurons of the cerebellum than iCb injection. Statistical comparison confirmed that both strategies prevented cerebellar pathology (motor deficits,

Fig. 3. iCb and CM injections of AAV9-hASM promote ASM expression and prevent molecular and cellular pathology in the cerebellum of ASM-KO mice. (**A**) Immunofluorescence images of hASM expression in Purkinje cells (indicated by asterisks) after iCb and CM injection of AAV9-hASM. ML, molecular layer; PCL, Purkinje cell layer; and GL, granular layer. (**B**) Phenotypic analysis of AAV9-hASM transduced cells in the cerebellum of iCb and CM AAV9-hASM–injected ASM-KO mice. Brain sections were costained in green against hASM and in red against neuronal (MAP2), astrocytic (GFAP), or microglia (Iba1) markers. Asterisks depict examples of cells coexpressing hASM and the cell type–specific marker. (**C**) Western blot analysis of hASM expression in cerebellar homogenates from ASM-KO mice injected with aCSF and iCb or CM AAV9-hASM. Graph shows mean ± SEM cerebellar hASM amount normalized to glyceraldehyde-3-phosphate dehydrogenase (GAPDH) ($n = 4$ per group). One-way ANOVA followed by Bonferroni post hoc. (**D**) Mean ± SEM SM concentration in cerebellar homogenates from WT and ASM-KO mice after receiving iCb or CM injection of aCSF or AAV9-hASM ($n = 3$ to 6 per group). Two-way ANOVA followed by Bonferroni (iCb) and Games-Howell (CM) post hoc. (**E**) Immunofluorescence staining against lysosomal Lamp1 in Purkinje cells (depicted by white dot lines) after aCSF or AAV9-hASM in iCb or CM injection in WT and ASM-KO mice. Graphs show mean ± SEM size of lysosomes in Purkinje cells after aCSF or AAV9-hASM iCb or CM injection in WT and ASM-KO mice ($n = 3$ to 6 per group). Two-way ANOVA followed by Bonferroni post hoc. (**F**) Purkinje cell density analysis by immunofluorescent staining of calbindin in the posterior lobe of the cerebellum after aCSF or AAV9-hASM iCb or CM injections in WT and ASM-KO mice. Graphs show mean ± SEM number of Purkinje cells after aCSF or AAV9-hASM iCb or CM injections in WT and ASM-KO mice ($n = 3$ to 6 per group). Two-way ANOVA followed by Bonferroni (iCb) and Games-Howell (CM) post hoc. DAPI (4',6-diamidino-2-phenylindole) staining in blue identifies the cell nuclei in the different panels. Scale bars, 50 μm for (A) and (B); 10 μm for (E); and 100 μm for (F). *$P < 0.05$, **$P < 0.005$, and ***$P < 0.001$.
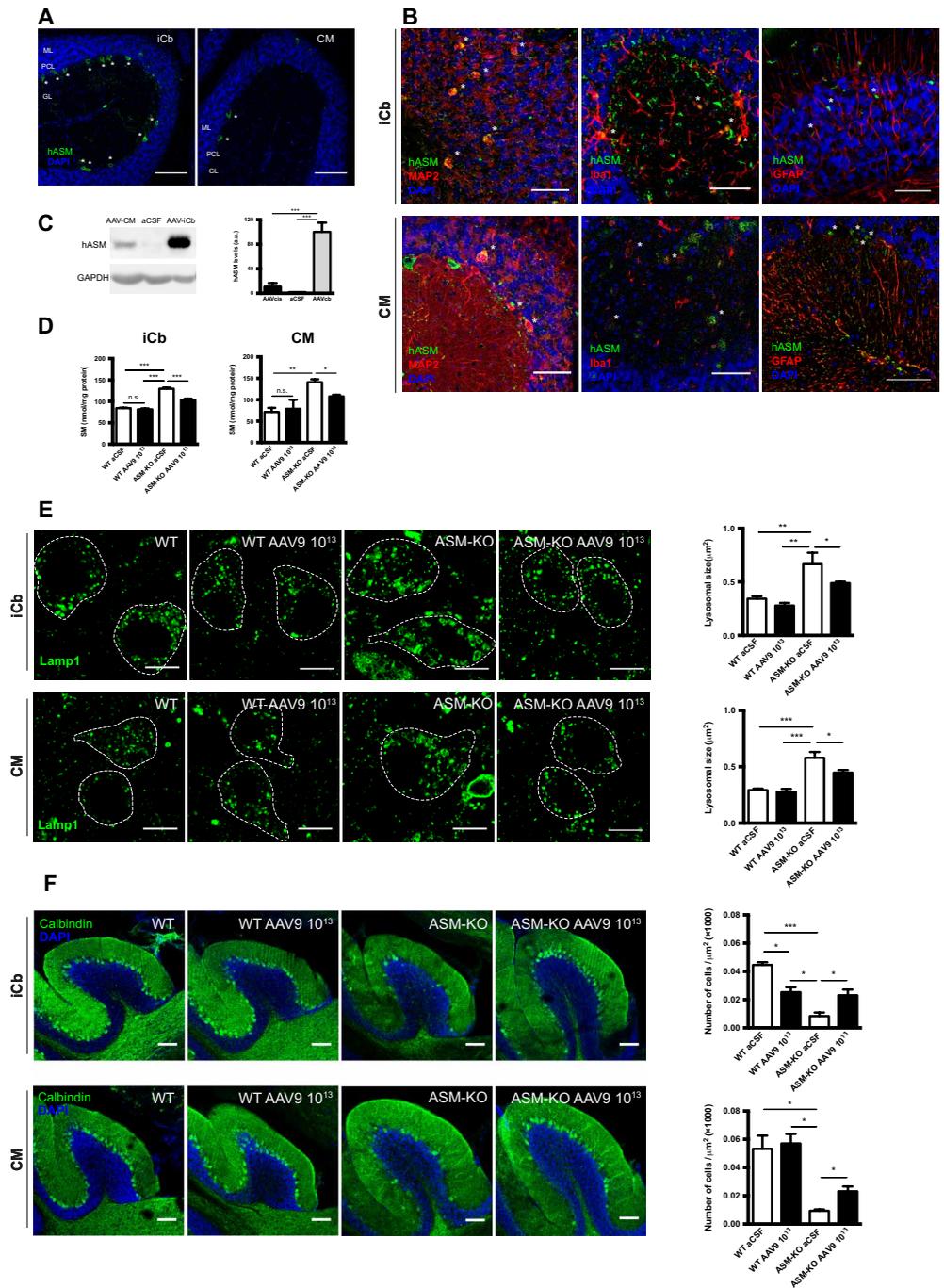
increased SM amount, and neurodegeneration) in ASM-KO mice to a similar extent (fig. S8). However, CM injection did not adversely affect Purkinje cell survival in WT mice (Fig. 3F), nor did it promote gliosis in contrast to iCb injection (Fig. 4 and fig. S5).

CM, but not iCb, injection of AAV9-hASM ameliorates pathology in the cortex and hippocampus of ASM-KO mice

Another goal of the AAV9-hASM CM injection was to reduce pathology in multiple brain regions, an observation not seen previously with direct brain delivery of hASM by AAV-based technology

(*23*, *24*). We analyzed hASM expression in areas close to the injection site as well as in distal regions by immunohistochemistry with a specific anti-hASM antibody. hASM-positive cells, costained with NeuN, were detected in the cortex and hippocampus of ASM-KO mice after CM injection of AAV9-hASM (Fig. 5A). No hASM-positive cells were found in the cortex and hippocampus of iCb-injected ASM-KO mice (fig. S9). Consistent with these findings, AAV9-hASM caused the reduction of SM concentration in cortical extracts of ASM-KO mice after CM injection, but not after iCb, compared to those that received aCSF injections (Fig. 5B). We could not detect SM reduction

Fig. 4. iCb, but not CM, injection of AAV9-hASM promotes inflammation in the cerebellum of ASM-KO mice. (**A**) Analysis of cerebellar astrocytes by immunofluorescent staining of GFAP in aCSF- and AAV9-hASM iCb- or CM-injected WT and ASM-KO mice. Graphs show mean ± SEM GFAP-associated intensity in aCSF or AAV9-hASM iCb- or CM-injected WT and ASM-KO mice ($n = 4$ per group). Two-way ANOVA followed by Bonferroni post hoc. (**B**) Cerebellar microglia analysis by immunofluorescent staining of Iba1 in aCSF or AAV9-hASM iCb- or CM-injected WT and ASM-KO mice. Graphs show mean ± SEM iba1$^+$ cell density in aCSF or AAV9-hASM iCb- or CM-injected WT and ASM-KO mice ($n = 4$ per group). Two-way ANOVA followed by Bonferroni post hoc. DAPI staining in blue identifies the cell nuclei in the different panels. Scale bars, 100 μm for (A) and 50 μm for (B). *$P < 0.05$, **$P < 0.005$, and ***$P < 0.001$.
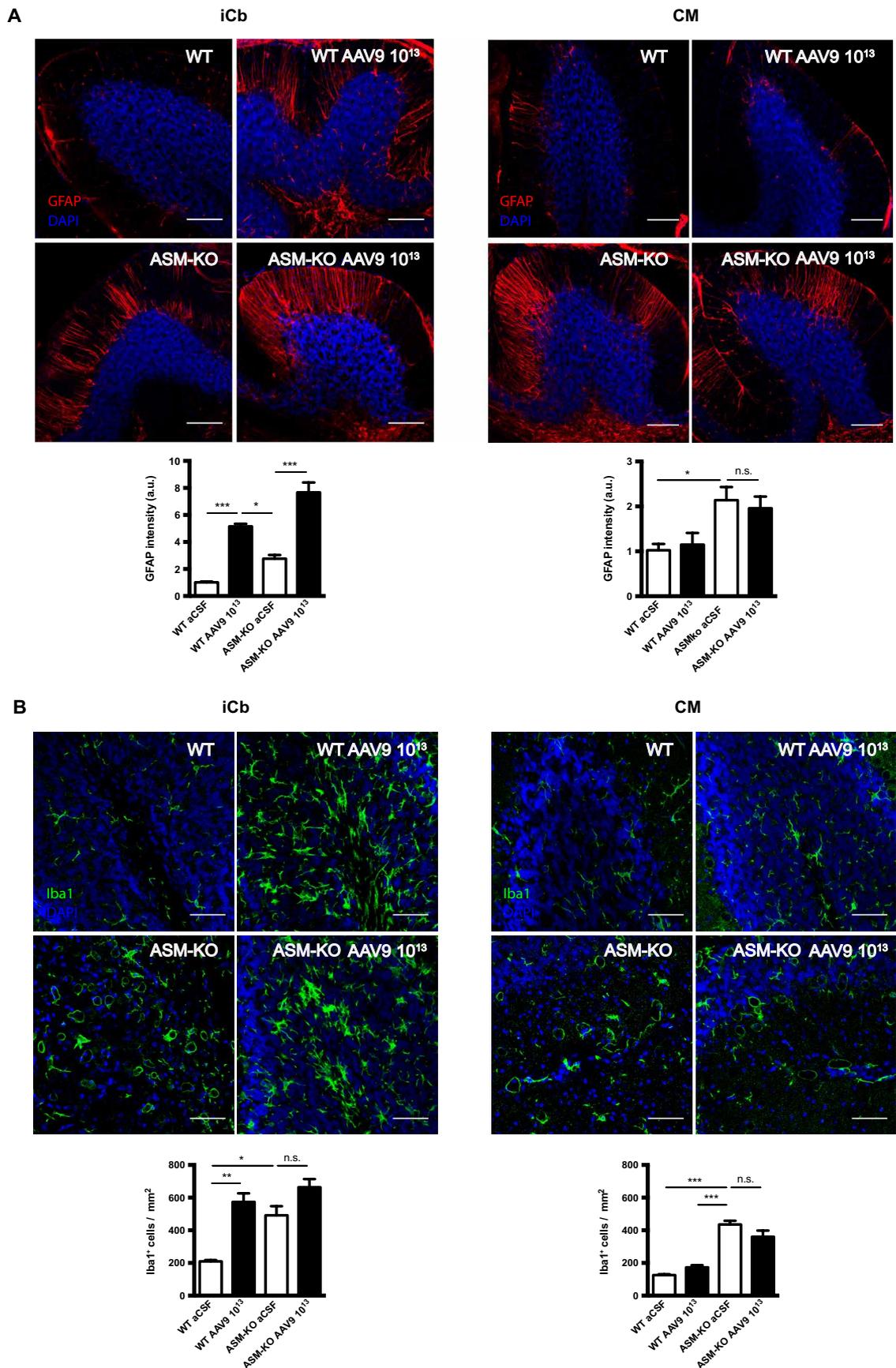
Samaranch et al., Sci. Transl. Med. **11**, eaat3738 (2019)   21 August 2019

7 of 15

in the hippocampus of ASM-KO mice after AAV9-hASM CM injection (Fig. 5C), but these mice showed improvements in hippocampus-dependent memory in the Y-maze test. They spent more time (45% of the total) exploring the novel arm compared to aCSF-injected ASM-KO mice (33% of the total, reflecting no discrimination between the three arms) (Fig. 5D). No changes in hippocampal SM concentration and memory were observed after iCb injection in ASM-KO mice or in WT mice (Fig. 5, C and D).

To determine whether CM injection of AAV9-hASM elicited hASM expression in deeper brain structures, we immunostained for hASM throughout the rostrocaudal axis. Although less abundant than in cortex and hippocampus, scattered hASM-positive cells were found in the hypothalamus, thalamus, and basal ganglia. More hASM-positive cells were found in the spinal cord (fig. S9).

CM injection of AAV9-hASM prevents liver pathology in ASM-KO mice
It has been recently shown that AAV9 can cross the blood-brain barrier into the CNS from the circulation (30) and migrate from the CNS back into the blood (29). Therefore, we tested whether AAV9-hASM delivered into the CSF injection had beneficial effects in peripheral organs, like the liver, that are heavily affected by NPD-A pathology. As expected, liver damage was evident in ASM-KO mice injected with aCSF, showing a 1.5-fold higher SM compared to WT mice (Fig. 6A). SM amount was not increased in the ASM-KO mice injected with AAV9-hASM in CM compared to WT mice (Fig. 6A). No changes were observed in SM amount in WT mice after aCSF or AAV9-hASM injection into the CM (Fig. 6A). AAV9-hASM injection also prevented liver inflammation. Active macrophages, reflected by amoeboid morphology, were found in the liver of aCSF-injected ASM-KO mice (Fig. 6B), whereas normal morphology, similar to WT mice, was found in macrophages of ASM-KO mice after AAV9-hASM injection into CM (Fig. 6B). These findings suggested a peripheral effect of the viral vector. To determine whether the therapeutic outcome in liver pathology could be due to transduction of this organ, we assessed for the presence of the viral vector genome. Quantitative polymerase chain reaction (PCR) analysis of DNA from liver extracts detected the mRNA of housekeeping genes such as glyceraldehyde-3-phosphate dehydrogenase and β-glucuronidase but not of hASM (fig. S10), suggesting the absence of a direct viral transduction of the hepatocytes. However, we did find ASM activity in plasma. AAV9-hASM CM injection increased ASM activity 1.26-fold in plasma compared to the baseline in ASM-KO mice that received aCSF injection (Fig. 6C). ASM activity in plasma of the AAV9-hASM–injected ASM-KO mice was 11.3-fold lower than in plasma of aCSF-injected WT mice (11.6 and 132.2 pmol ml^{-1} hour^{-1}, respectively) (fig. S11). Given the positive effects of AAV9-hASM CM injection observed after 2 months of treatment, we extended the treatment in a group of WT and ASM-KO mice to determine the effects on survival. Although all aCSF-injected ASM-KO mice died before 39 weeks of age (mean survival, 265 ± 5 days), none of the AAV9-hASM CM-injected ASM-KO or WT mice had died at that time (Fig. 6D).

DISCUSSION
NPD-A is a rare autosomal recessive disease emblematic of a number of LSD in which the impaired activity of specific lysosomal enzymes leads to the accumulation of toxic metabolic products and results in widespread disease and curtailed life span. Cumulatively,

these LSD occur at about 1 in 8000 live births and are often characterized by serious neurological deficits. Because replacement of the defective gene (or enzyme) is the obvious solution, direct brain gene therapy has been proposed as a feasible therapeutic strategy (20), especially because systemic infusion of the recombinant enzymes does not treat CNS disease due to the inability of the enzyme to cross the blood-brain barrier (15). Several characteristics make NPD-A especially suitable for gene therapy. A low residual activity of the ASM enzyme in patients (~5 to 10% of normal activity) seems to be enough to prevent the neurological symptoms of NPD (1, 2). This suggests that modest restoration of the missing ASM activity in the brain might have therapeutic effects in patients with NPD-A, especially in the neuropathologic phenotype, and supports the idea that successful gene therapy might not require massive overexpression of the ASM transgene. Moreover, ASM is a secreted enzyme that can be taken up by cells, thus enabling cross-correction of noninfected cells by neighboring transduced cells (bystander effects).

Despite these advantageous characteristics, previous gene therapy attempts in rodents and NHP have revealed a series of challenges for NPD-A treatment. Metabolites of SM, like ceramide and its downstream products, sphingosine and sphingosine-1-P, can trigger calcium imbalance, aberrant intracellular signaling, inflammation, and cell death (37–40). Work in NHP has shown that high focal ASM expression boosted SM metabolites, triggering deleterious inflammatory responses (27). However, these adverse effects were likely due to reaching the maximum-tolerated dose and may be eliminated by dose de-escalation. Moreover, because ASM is a ubiquitous enzyme, its deficiency affects both glia and neurons in all brain areas (36). Therefore, broad spatial and cellular distribution in this organ would be necessary for an optimal therapeutic efficacy. Together, these findings suggest that achieving modest, but global, ASM activity in the brain should therefore be goals of a gene therapy for NPD-A. The serotype of the AAV vector and the route of delivery are key determinants in meeting these goals (29, 33). Our results demonstrate that CM injection of AAV9-hASM elicits broad brain expression of ASM in a sufficient number of glia and neurons for therapeutic benefit. This strategy ameliorates molecular and cellular NPD-A brain pathology by reducing SM amount and correcting lysosomal dysfunction, yet improving neuronal survival without triggering an inflammatory response in a mouse model. The effects of AAV9-hASM in the cerebellum after CM injection of AAV9-hASM are comparable to those obtained after iCb injection, and both strategies result in improved motor abilities in the ASM-KO mice. However, CM proved to be a safer injection, avoiding the deleterious events observed with the iCb procedure, such as gliosis in the ASM-KO cerebellum and Purkinje cell loss in the WT mice. It is likely that these effects are due to high focal ASM expression induced by the iCb injection, leading to a sudden "burst" of pro-inflammatory SM metabolites such as ceramide. Thus, moderate ASM expression achieved by CM injection of AAV9-hASM would probably prevent such toxic effects, and its broader distribution also makes this strategy a more suitable choice to treat brain NPD-A pathology than the iCb injection. CM injection, but not iCb, also resulted in cortical and hippocampal hASM expression and reduced SM amount in these brain regions. Although injection of the vector into mouse CM resulted in low hASM expression in these regions, it was enough to evince functional benefits as demonstrated by the improved hippocampus-dependent memory in the ASM-KO–treated mice. This is consistent with the view that quite low ASM is sufficient to prevent brain
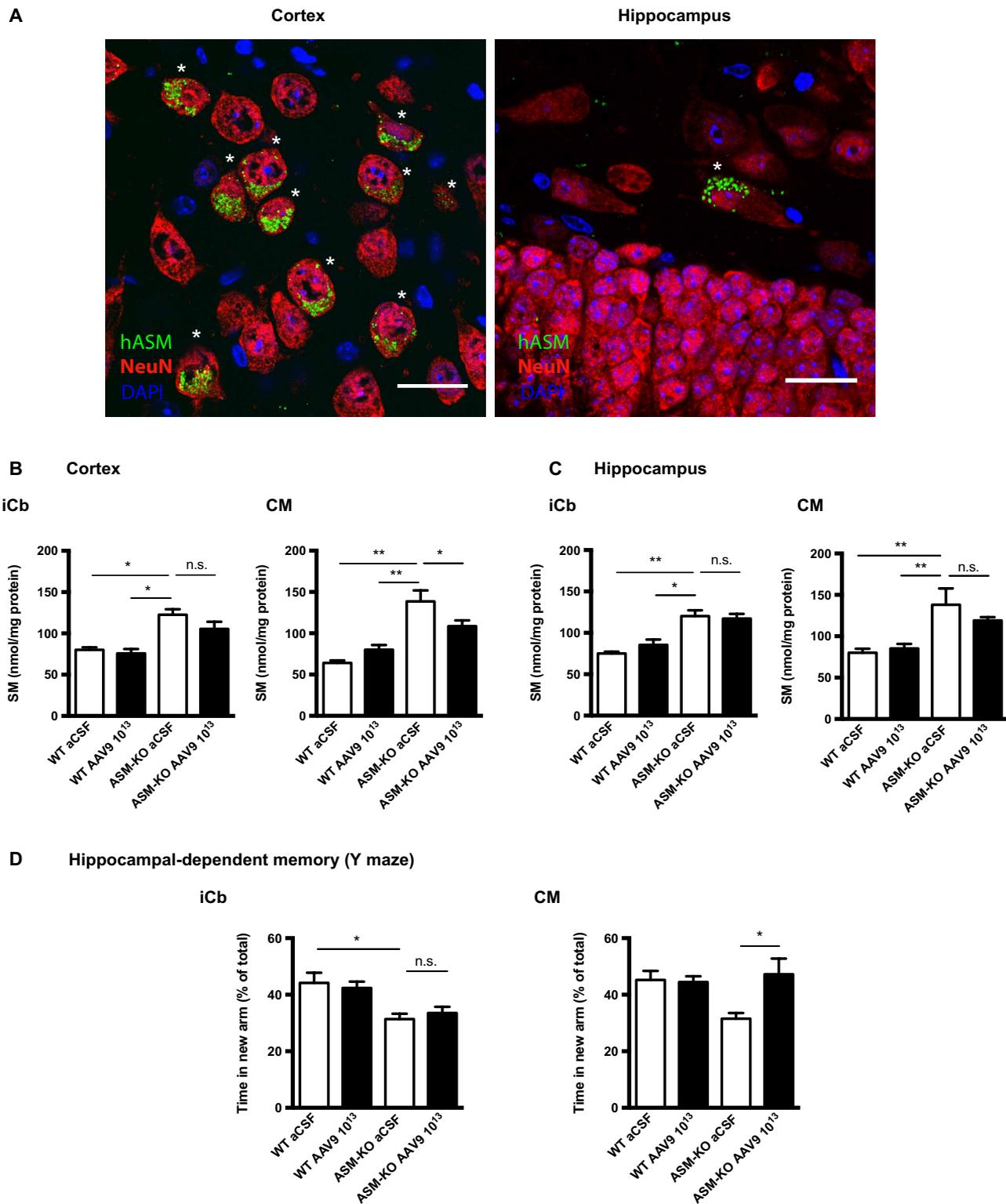
Fig. 5. CM, but not iCb, injection of AAV9-hASM affects the cortex and hippocampus in ASM-KO mice. (**A**) Cortex and hippocampus from ASM-KO mice stained for hASM and the neuronal marker NeuN after CM injection of AAV9-hASM. Asterisks indicate hASM-positive cells. DAPI staining in blue identifies the cell nuclei. (**B**) Mean ± SEM SM concentration in cortical homogenates from WT and ASM-KO mice iCb or CM injected with aCSF or AAV9-hASM (*n* = 4 to 6 per group). Two-way ANOVA followed by Bonferroni post hoc. (**C**) Mean ± SEM SM concentration in hippocampal homogenates from WT and ASM-KO mice iCb or CM injected with aCSF or AAV9-hASM (*n* = 3 to 6 per group). Two-way ANOVA followed by Bonferroni post hoc. (**D**) Mean ± SEM time spent in the novel arm of the Y maze spontaneous alternation test in WT and ASM-KO mice iCb or CM injected with aCSF or AAV9-hASM (*n* = 3 to 7 per group). Two-way ANOVA followed by Bonferroni post hoc. Scale bars, 25 μm. *$P < 0.05$ and **$P < 0.005$.
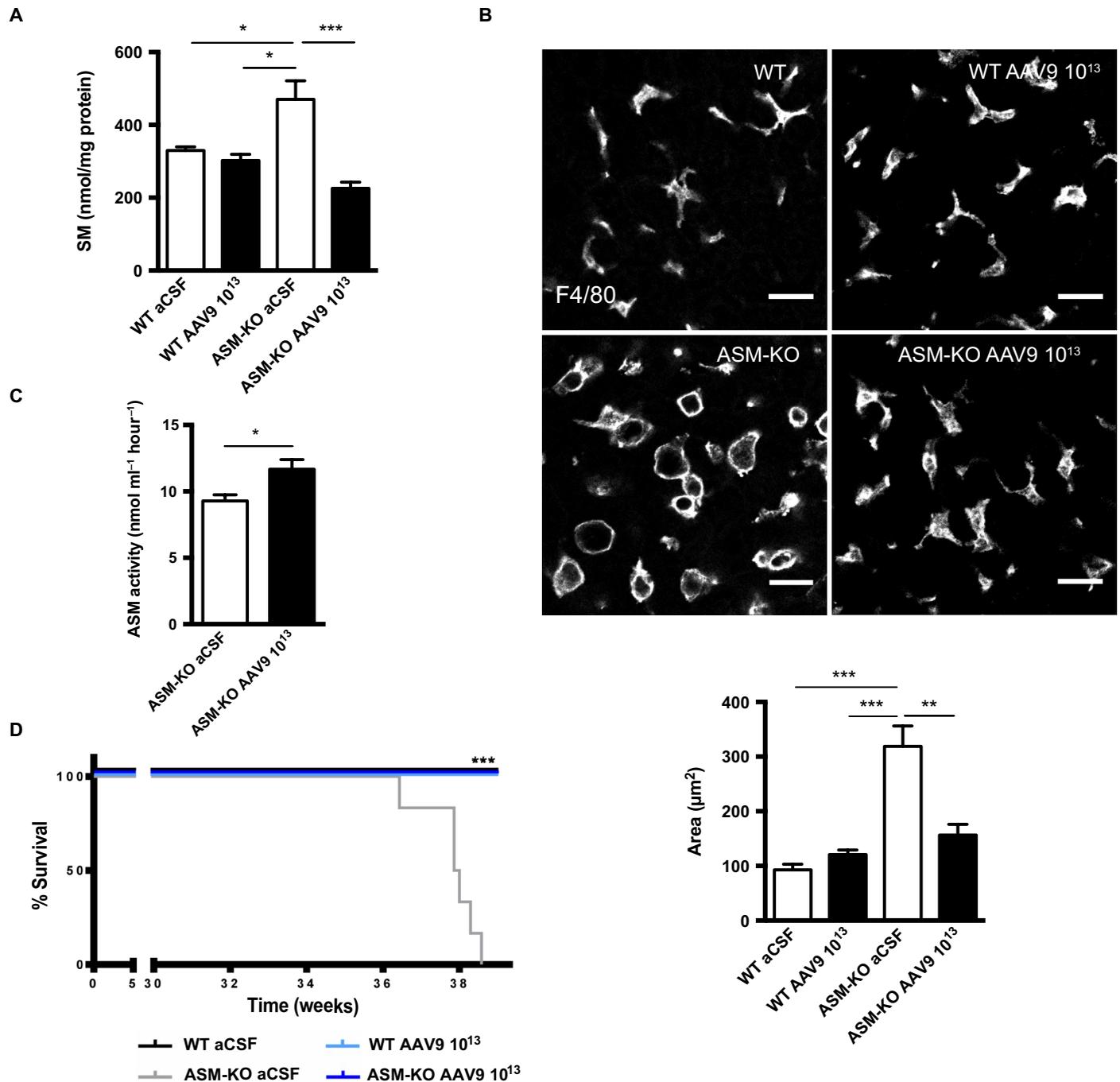
Fig. 6. CM injection of AAV9-hASM increases ASM activity in plasma and improves liver pathology in ASM-KO mice. (**A**) Mean ± SEM SM concentration in the liver of WT and ASM-KO mice CM injected with aCSF or AAV9-hASM ($n = 5$ to 8 per group). Two-way ANOVA followed by Bonferroni post hoc. (**B**) Liver from WT and ASM-KO mice injected into CM with aCSF or AAV9-hASM stained for the specific macrophage marker F4/80. Graph shows mean ± SEM area of macrophages ($n = 3$ to 4 per group). (**C**) Fold increase in ASM activity in plasma of ASM-KO mice injected into CM with AAV9-hASM over the basal values in aCSF-injected ASM-KO mice ($n = 7$ per group). Mann-Whitney U test. (**D**) Survival curve showing the percentage of WT and ASM-KO mice, CM injected with aCSF or AAV9-hASM, at the indicated time in weeks after birth ($n = 6$ per group). Mantel-Cox test. Scale bars, 25 μm. *$P < 0.05$, **$P < 0.005$, and ***$P < 0.001$.

pathology if broadly distributed. We showed that CM injection of AAV9-hASM has a substantial impact in the spinal cord and also reaches deep brain subcortical areas like thalamus, hypothalamus, and basal ganglia, albeit to a lesser extent. Administration of vector into the CSF through the lateral ventricle may enhance hASM

expression in subcortical areas (*41*). Our study paves the way to test this possibility.

Applicability of this therapy to human infants is another major concern in the NPD-A field. Although multiple surgical improvements are currently under development with miniaturized delivery devices

(42), invasive cerebral surgeries required for direct brain injections are more challenging in infants. In contrast, CM injection is a much less invasive technique that is used regularly in the clinic to collect CSF for diagnostic purpose and could be used easily in infants by computerized tomography (CT)–guided delivery. Recently, we also developed an MR-based guidance and injection monitoring system for CSF delivery of viral vectors that should enhance the precision of this type of delivery (43).

In addition, our study in NHP confirms that AAV9-hASM injection in CM elicits broad hASM expression in a larger brain and spinal cord, comparable in size to a human infant. The absence of any behavioral adverse effects, even 3 months after injection, and the absence of immune infiltrates in the brain parenchyma and vascular lumina confirm CM as a relatively benign procedure that avoids overtransduction, preventing areas with focally excessive ASM activity that would move the balance to downstream products of the SM metabolic pathway that can induce neuronal apoptosis above a certain threshold (39). Neutralizing antibodies were evaluated in the NHP study, and total IgG increased 1 and 3 months after treatment in peripheral blood and CSF. NHPs in our study remain seronegative according to the criteria used in clinical trials with antibody titers lower than 1:1200 (34).

An important consideration in the NPD-A treatment strategy is the need for early intervention with a very narrow window for therapeutic effect. NPD-A is most frequently diagnosed in children when symptoms appear at 3 to 6 months of age and patients rarely survive beyond 3 years (3). Our results in ASM-KO mice show that CM injection of AAV9-hASM is effective even after disease onset, and benefits become evident after a relatively short period. At 7 weeks of age, injected ASM-KO mice already showed SM increases in brain tissue, as well as Purkinje cell loss and progressive motor deficits. However, AAV9-hASM treatment halted further disease progression of neuropathology.

Although the neurodegenerative course is the most devastating feature of NPD-A, the peripheral pathology also needs to be addressed. Vascular delivery of AAV9 results in a mixture of neuronal and astrocytic transduction (31) that seems to depend on the age of the animal (30). However, this strategy has more off-target effects, dilutes the vector dose directed to the nervous system, increases risk of abrupt generation of neutralizing anti-AAV antibodies, and requires larger volumes of viral vector than AAV9 CSF delivery (29). On the other hand, the ability of AAV9 to cross the blood-brain barrier may enable a systemic impact after injection of CSF. Our results showing ASM activity in plasma from CM-injected ASM-KO mice also correlates with a reduction of SM amount and reduction of inflammation in the liver. The negative outcome of our attempts to detect viral genomes in the liver would argue against transduction of this organ and in favor of hASM enzyme leakage into the circulation to explain the therapeutic effects. In that respect, we propose that the transduction of the ependymocytes that line the ventricular system could provide an active enzyme replacement that would sustain the therapeutic benefit (44, 45). Accordingly, enzyme would reach the subarachnoid space and would be internalized throughout multiple brain regions along perivascular spaces for brain enzyme replacement. Moreover, enzyme would be also capable to pass through the arachnoid villi and reach the peripheral vasculature for systemic enzyme replacement throughout the paravascular pathway (46), a CSF/interstitial fluid clearance mechanism to eliminate extracellular solutes from the interstitial compartments of the brain and spinal cord. In our hands, although the very low ASM activity

found in rodent plasma raises concerns regarding long-term efficacy for peripheral symptoms, and further investigation would be needed, our NHP data support this hypothesis by the extensive transduction found in the ventricular system, choroid plexus, and surrounding areas (fig. S12), and the increased expression of hASM enzyme found in the liver from treated NHPs. Fortunately, ERT by intravenous injection of rhASM seems to be successful in treating systemic, but not CNS, symptoms in ASM-KO mice and in patients with NPD-B (15, 16). A phase 2 clinical trial is currently ongoing in adult and pediatric populations (NCT02004704). We, therefore, believe that the combination of AAV-based gene therapy into CM followed by ERT offers an optimal approach for the comprehensive treatment of NPD-A. In our opinion, this study would guide clinical development not only for NPD-A, for which no treatment is currently available, but also for other monogenic brain LSD, having a substantial impact on public health and reinforcing the therapeutic value of AAV-based genome editing.

Effective gene therapy in patients with NPD-A presents some challenges. First, diagnosis is generally made on the basis of symptoms in children 3 to 6 months of age when disease has already progressed. Our data indicate that, in mice, such symptoms may be substantially ameliorated even after pathology is present. However, we cannot be sure that humans will respond similarly. Second, the liver and spleen are severely affected by NPD-A and, although we saw some modest signs of ASM expression in treated mouse liver, this may be far from a fully corrective effect in humans, thereby necessitating ERT in addition to gene therapy. We have not investigated this combined therapy in the ASM-KO mouse model yet. Further studies will be required to determine whether this combined therapy presents substantial problems.

MATERIALS AND METHODS
Study design
The goal of this study was to assess safety, in NHP, and dose-response efficacy, in ASM-KO mice, of cisterna magna delivery of a recombinant AAV9 vector encoding hASM. The sample size for each experiment is included in the figure legends. The number of mice used was selected on the basis of previous phenotyping analyses conducted in the same model and calculating the statistical power of the experiment. Mice were genotyped and, according to the genotype, randomly assigned to the experimental groups. No outliers were excluded in the study. Sample collection, treatment, and processing information are included in Results and Materials and Methods. Investigators assessing and measuring results were blinded to the intervention. Primary data are reported in data file S1.

Vector production and infectivity assessment in cultured neurons
All the viruses injected in the present study were manufactured by recombinant baculovirus (rBAC) technology in insect cells as previously described (47). Briefly, the AAV viral genome was cloned into a series of rBAC to facilitate the viral genes required for propagation (*rep* and *cap*). First, two separate transcription units via partial duplication of *rep* coding sequences were expressed in one rBAC. Second, the AAV virion coat proteins from a modified AAV *cap* gene were expressed in another rBAC, and last, a third baculovirus expression cassette containing the cytomegalovirus (CMV) promoter, a chimeric CMV/β-globin intron, the human *ASM* gene (for full

capsids), and the human growth hormone polyadenylation site was cloned into the AAV vector plasmid between the two inverted terminal repeat sequences. These rBACs were used to transiently transfect the sf9 insect cells to produce the empty AAV9 vector and the one encoding human ASM complementary DNA (cDNA) (AAV9-CMV-hASM). Viral particles of the AAV9-hASM vector were assessed for infectivity and enzyme secretion in primary cultures of cortical neurons derived from ASM-KO mice. AAV9-hASM was added to the culture media at a final concentration of 1×10^{12} vg/ml. After 6 days of incubation, neurons and media were collected, and the expression of hASM was analyzed by Western blot with an antibody that recognizes human but not mouse ASM (rabbit anti-ASM, 1:1000; sc-11352 Santa Cruz) (fig. S13).

Animals included in this study
Nonhuman primates
Three adult cynomolgus macaques (*Macaca fascicularis*; ~3.0 to 9.0 kg) were included in this study. Before vector administration, animals were tested for the presence of anti-AAV9 antibodies as previously described (*29*), and all were seronegative with antibody titers lower than 1:400. Two animals received a single dose of vector; an un-injected animal was used as control. After CSF delivery, veterinary personnel monitored animals daily until necropsy at 30 or 91 days, when animals were tested again for antibodies. All procedures were carried out in accordance with the UCSF Institutional Animal Care and Use Committee (San Francisco, CA).

Mice
A breeding colony was established from ASM heterozygous C57BL/6 mice donated by E.H. Schuchman (Mount Sinai School of Medicine, New York). Male and female WT and ASM-defective mice (ASM-KO) littermates were identified by PCR performed on DNA isolated from the tail (*10*) and were randomly assigned to experimental groups. Internal review boards at the Centro Biologia Molecular Severo Ochoa (CBMSO) and Consejo Superior Investigaciones Científicas (CSIC) approved all of the procedures involving the use of mice that were performed in accordance with specific European Union guidelines for the protection of animal welfare (Directive 2010/63/EU). The authors adhere to the NIH Guide for the Care and Use of Laboratory Animals.

Vector delivery
Nonhuman primates
Animals received a single injection of vector into the CM as previously described (*29*). Briefly, after induction of anesthesia, the animal's head was placed in a stereotactic frame and flexed in a prone position. The back of the neck was shaved and cleaned with Nolvasan solution and alcohol. A 3-ml syringe attached to a 1-inch 23-gauge spinal needle was mounted onto a stereotactic micromanipulator. The needle was manually guided to the craniocervical junction. The micromanipulator was used to guide the needle through the atlanto-occipital membrane to the CM. To verify correct positioning, a small volume of CSF was aspirated. A three-way stopcock connected to the syringe was then adjusted to allow infusion of the vector at 0.5 ml/min via an infusion pump (3500 Medfusion; Strategic Applications). After completion of the vector infusion, the line was flushed with saline. A small volume of CSF was aspirated to verify that the needle remained in the CM. Five minutes after infusion, the needle was slowly removed by means of the micromanipulator. Subsequently, animals were maintained on a warming blanket, and vital signs were monitored by a veterinary technician. They were then returned to

their home cages and observed for any sign of discomfort or distress until fully recovered from anesthesia. Clinical evaluations were performed and recorded by trained veterinary technicians twice daily for 5 days.

Mice
Animals were injected into the CM as in NHP, although some modifications were necessary. Briefly, mice were anesthetized with isoflurane, and the head was placed in a stereotaxic frame in a prone position. A 26-gauge needle was connected to a 3-ml syringe by a 22-gauge PinPort (PNP3F22-50, Instech Laboratories Inc., PA) and mounted in a stereotactic arm. Then, the needle was manually guided into the CM. Accurate location was verified by CSF presence in the needle hub by pulling the syringe's plunger. The 3-ml syringe was detached, and custom-made fused silica tubing connected to a PinPort injector attached to a Hamilton glass syringe was connected to the needle. Ten microliters of aCSF or AAV9-hASM or empty vector diluted in aCSF was injected by a pump (Micro4, World Precision Instruments) at 1.4 μl/min. One minute after finishing the injection, the needle was retracted, and gentle pressure was applied in the injected area. A separate group of mice received iCb injections, in which 2 μl of aCSF or virus diluted in aCSF was injected at 0.2 μl/min by a glass micropipette into the deep cerebellar nucleus of both hemispheres [anterior-posterior (AP): −5.75; medial-lateral (ML): −1.8; dorso-ventral (DV): −2.6 mm] of deeply anesthetized animals. In both cases, after surgery, mice were placed in a recovery chamber and were monitored until fully recovered. Then, mice were transferred to their home cages and were monitored daily by trained personnel during the first week after injection and then weekly until the end of the study.

Motor and memory analysis in mice
Motor testing was performed in an accelerating rotarod apparatus (Ugo Basile, 47650 Mouse Rotarod NG), on which the mice were trained for 2 days at a constant speed: four times at 4 rpm for 1 min on the first day and four times at 8 rpm for 1 min on the second day. On the third day, the rotarod was set to progressively accelerate from 4 to 40 rpm for 5 min, and the mice were tested four times. During the accelerating trials, the latency to fall from the rod was measured.

The Y-maze spontaneous alternation test was performed as previously described (*48*). During the first training trial (8 min), the mice were allowed to explore only two arms (the initial arm and another arm), maintaining the third arm (novel arm) closed. After 1 hour, the mice were placed back in the same starting arm with free access to all three arms for 5 min. The time spent in the novel arm was counted and expressed as a percentage of the total exploration time.

Tissue collection and processing
Nonhuman primates
Animals were transcardially perfused with ice-cold phosphate-buffered saline (PBS). Brains were harvested and sliced into 3-mm coronal blocks in a brain matrix. Alternate unfixed brain blocks were quickly frozen in dry ice and stored at −80°C until ASM analysis. All other brain slices were postfixed by immersion in 4% paraformaldehyde/PBS overnight and then transferred to 30% (w/v) sucrose in PBS. A sliding microtome was used to cut serial 40-μm coronal sections for histological processing. All sections were stored in cryoprotectant solution until further use. Spinal cord from cervical, thoracic, and lumbar regions, and the liver were also fresh-frozen collected. Representative portions of tissue were snap-frozen or postfixed as previously indicated.

Mice

Animals were transcardially perfused with saline solution (0.9% NaCl), and the brain and liver were freshly dissected out. One brain hemisphere and a liver lobe were fixed overnight at 4°C in 4% paraformaldehyde/PBS and cryoprotected in 30% sucrose in PBS for 48 hours. Tissue was then frozen in optimal cutting temperature (Tissue-Tek, 4583 Sakura), and 30-μm sagittal sections were cut for histological analysis with a sliding microtome. The remaining brain hemisphere and another liver lobe were homogenized in MES buffer (20 mM MES, 150 mM NaCl, and 1 mM EDTA) for biochemical analysis.

SM analysis

Biochemical analysis of SM was performed in the brain and liver extracts by a modified enzymatic assay (5) from Hojjati and Jiang standard protocol (49). Briefly, 15 to 30 μg of brain homogenates was dried in the presence of the nonionic detergent Thesit (CAS number 9002-92-0, Sigma-Aldrich). SM was subsequently converted into choline by means of SM and alkaline phosphatase, and coupled to the production of fluorescence with choline oxidase, peroxidase, and homovanillic acid. A standard curve of SM (CAS number 85187-10-6, Sigma-Aldrich) diluted in chloroform was used to determine lipid concentration in the samples.

ASM activity assay

ASM activity was determined in CSF and plasma as previously described (50). Briefly, 3 μl of CSF or plasma was mixed with 3 μl of substrate buffer (200 μM boron-dipyrromethene (BODIPY)–labeled C12 SM, Thermo Fisher Scientific). This was then diluted with assay buffer [0.2 M sodium acetate (pH 5)] containing 0.2 mM $ZnCl_2$ and 0.2% Igepal CA-640. This mixture was incubated at 37°C for 1 to 3 hours, and the reaction was then stopped with ethanol. The hydrolytic product, BODIPY C12-ceramide, was detected and quantified by an Ultra Performance Liquid Chromatography system (Acquity UPLC H-class, Waters) fitted with an Acquity BEH amide, 2.1 mm by 50 mm, 17-mm column (Waters).

ASM enzyme-linked immunosorbent assay

Tissue concentrations of ASM were determined with a commercially available kit: Human SMPD1 ELISA Kit (abx572070, Abbexa). After slicing the brain into 3-mm blocks, tissue biopsies were collected from alternate frozen blocks (2.0-mm disposable biopsy punch; Robbins Instruments) in different regions of interest and stored at −80°C. Samples were later homogenized with a model 100 Fisher Science Dismembrator in 250 μl of ice-cold buffer containing 100 mM potassium phosphate (pH 7.8), 0.2% Triton X-100, and protease inhibitors (Complete Mini, Roche), and homogenates were centrifuged at 13,000g for 15 min. The supernatant solutions were collected and ASM concentrations were measured by ELISA. Absorbance was measured with an ELx808 microplate reader (BioTek) according to the manufacturer's protocol. The concentration of ASM in tissue extracts was then calculated by reference to a standard curve and expressed as nanograms of ASM per milligram of total tissue protein (DC Protein Assay Kit, Bio-Rad).

Histology

Nonhuman primates

A monoclonal antibody against hASM (biotinylated mouse anti-hASM, 1:400, a gift from Sanofi, Cambridge, MA, USA) was used for transgene detection. This antibody is not species-specific and detects both endogenous and AAV-mediated de novo enzyme. However, the physiological amount of endogenous ASM is very low, and vector-driven ASM expression is easily distinguishable, as we have previously demonstrated (27, 28). On the basis of reports of adverse effects after focal ASM overexpression (27), H&E staining and immuno-staining against CD4 (rabbit anti-CD4; 1:150, CM 153 BK, Biocare), CD8 (rabbit anti-CD8; 1:50, CRM311, Biocare), CD68 (mouse anti-CD68; 1:100, M0814, DAKO), GFAP (mouse anti-GFAP, 1:100,000; MAB360, Millipore), Iba1 (rabbit anti-Iba1, 1:1000; CP290C, Biocare Medical), and MHC-II (mouse anti-MHCII, 1:300; M3887-30, US Biological) were performed to study any immunological response to exogenous ASM. Calbindin (rabbit anti-calbindin, 1:100,000; CB-38a), a widely recognized marker of Purkinje cell integrity, was also completed to evaluate cerebellar pathology (32). Lysosomal/endosomal distribution pattern was assessed with double-label immunofluorescence for ASM (mouse anti-hASM, 1:100, Sanofi) and a lysosomal marker, LAMP-1 (rabbit anti-LAMP1, 1:200, D2D11, Cell Signaling Technologies). Vector-mediated ASM expression was quantified throughout the cortical cerebrum and cerebellum with infrared (IR) immunofluorescence, which has been validated as a means of protein quantification (51). Representative sections from the cortex, cerebellum, hippocampus, and thalamus were stained for ASM (mouse anti-hASM, 1:100, Sanofi) followed by an IR secondary antibody (goat anti-mouse IgG, 1:1000, IRDye 800CW, Li-Cor). Sections were then scanned on an Odyssey CLx imaging system. Scanned images had various cortical regions delineated using the Image Studio Lite software package. Delineation of the desired region of interest yielded a signal value. Each signal value was then normalized to the area of the region of interest (ROI), and then the signal-to-area ratio was used to compare different time points.

Mice

Brain sections were incubated overnight at 4°C with antibodies against calbindin D-28k (mouse monoclonal anti-calbindin, 1:200, McAB 300), hASM (biotinylated mouse anti-hASM, 1:100; Genzyme), GFAP (rabbit polyclonal anti-GFAP, 1:500, Dako), Iba1 (rabbit polyclonal anti-Iba1, 1:200, Wako), Lamp1 (rat monoclonal anti-Lamp1, 1:500, DSHB), MAP2 (chicken polyclonal anti-MAP2, 1:500, BioLegend), or NeuN (rabbit polyclonal anti-NeuN, 1:1000, Merck Millipore). Liver sections were incubated with F4/80 antibody (rat monoclonal anti-F4/80, 1:200, Abcam). Corresponding Alexa-conjugated secondary antibodies (1:1000, Invitrogen) were used. Last, the sections were incubated for 10 min with 4′,6-diamidino-2-phenylindole (1:5000, Calbiochem), washed, and mounted with Prolong Gold Antifade (Invitrogen). Images were obtained on a confocal LSM710 microscope (Carl Zeiss AG). For the quantification of lysosomal size in Purkinje cells, lysosomes were stained using an anti-Lamp1 antibody, and their size was quantified by ImageJ software. No size or circularity exclusion was applied, and the same threshold was used in all images. The Purkinje cell soma was identified by calbindin staining. Nissl staining was performed in cerebellar sections by incubation in 1% cresyl violet for 5 min followed by washing with water and dehydration with increasing concentrations of ethanol (from 96 to 100% ethanol), which was replaced by two final rinses with xylene.

Quantitative PCR in liver extracts

Total RNA from liver homogenates was extracted with TRIzol Reagent (Ambion/RNA Life Technologies Co.) and chloroform following the TRIzol Reagent protocol from Sigma-Aldrich. RNA was quantified by absorbance at 260 nm with a NanoDrop One

(Thermoscientific, Thermo Fisher Scientific Inc.). Retrotranscription to cDNA was performed with the RevertAid H Minus First Strand cDNA Synthesis Kit from Thermo Fisher Scientific. Then, 10 ng of synthesized cDNA was used to perform the qPCR with GoTaq qPCR Master Mix (Promega Co.) in ABI PRISM 7900HT SDS (Applied Biosystems, Life Technologies Co.). For the detection of hASM vector transcripts, the following primers were used at 0.5 μM final concentration: hASMvect_fw: 5′-AGACACGTTTGAGGACATCA and hASMvect_rv: 5′-AAGCATGGCCGGGTACG (Sigma-Aldrich). Two housekeeping genes, GAPDH (glyceraldehyde-3-phosphate dehydrogenase) and GusB, were used as endogenous controls.

Statistics

Normality of the data was tested with the Shapiro-Wilk test. For two-group comparisons, the Mann-Whitney U test for nonparametric data or a two-sample Student's t test for data with parametric distribution was used. For multiple comparisons, two-way analysis of variance (ANOVA) followed by Bonferroni, LSD, or Games-Howell post hoc test was performed. For the survival data, the Mantel-Cox test was used. Normalized regional comparisons of ASM-IR immunoreactivity were compared by two-way ANOVA followed by Tukey's post hoc test. P values <0.05 were considered significant, and the statistical tests and sample size (n values) used in the experiments are specified in the figure legends. In the figures, asterisks indicate the P values: *P < 0.05, **P < 0.005, and ***P < 0.001. SPSS 20.0 software (IBM, Armonk, NY, USA) and GraphPad Prism 8.0b for Mac OS X software (GraphPad software, La Jolla, CA, USA) were used for the statistical analyses.

SUPPLEMENTARY MATERIALS

stm.sciencemag.org/cgi/content/full/11/506/eaat3738/DC1

Fig. S1. ASM colocalizes with the lysosomal marker Lamp1.

Fig. S2. AAV9-hASM CM injection does not promote immune response in brain tissue of NHP.

Fig. S3. Expression of hASM does not differ among cerebellar lobes in AAV9-hASM iCb- and CM-injected ASM-KO mice.

Fig. S4. Purkinje cell death is more evident in cerebellar lobes of AAV9-hASM iCb- compared to CM-injected ASM-KO mice.

Fig. S5. Astrocytosis and microgliosis are higher in cerebellar lobes of AAV9-hASM iCb- compared to CM-injected ASM-KO mice.

Fig. S6. AAV9-hASM iCb-injected ASM-KO mice show higher ceramide levels than AAV9-hASM iCM-injected ASM-KO mice.

Fig. S7. ASM-KO mice noninjected and CM injected with AAV9 empty vector or aCSF show similar behavioral, cellular, and molecular pathology.

Fig. S8. Statistical comparison of the effects of cerebellar iCb and CM injection in ASM-KO mice.

Fig. S9. CM injection of AAV9-hASM promotes hASM expression along the rostrocaudal axis.

Fig. S10. hASM mRNA is not detected in the liver of AAV9-hASM CM-injected ASM-KO mice by RT-PCR.

Fig. S11. ASM activity in plasma of aCSF-injected WT is higher than in ASM-KO AAV9-hASM CM-injected mice.

Fig. S12. CM injection results in a vast transduction of different components of the ventricular system and surrounding areas.

Fig. S13. AAV9-hASM infects primary cortical neurons of ASM-KO mice and elicits secretion of hASM.

Table S1. AAV9-hASM CM injection does not affect general health, appearance, and behavior of NHP as determined by monthly average of daily observations.

Data file S1. Primary data.

REFERENCES AND NOTES

1. E. H. Schuchman, The pathogenesis and treatment of acid sphingomyelinase-deficient Niemann–Pick disease. *J. Inherit. Metab. Dis.* **30**, 654–663 (2007).
2. E. H. Schuchman, The pathogenesis and treatment of acid sphingomyelinase-deficient Niemann-Pick disease. *Int. J. Clin. Pharmacol. Ther.* **47** (suppl. 1), S48–S57 (2009).
3. M. M. McGovern, T. Pohl-Worgall, R. J. Deckelbaum, W. Simpson, D. Mendelson, R. J. Desnick, E. H. Schuchman, M. P. Wasserstein, Lipid abnormalities in children with types A and B Niemann Pick disease. *J. Pediatr.* **145**, 77–81 (2004).
4. A. Berger, D. Rosenthal, S. Spiegel, Sphingosylphosphocholine, a signaling molecule which accumulates in Niemann-Pick disease type A, stimulates DNA-binding activity of the transcription activator protein AP-1. *Proc. Natl. Acad. Sci. U.S.A.* **92**, 5885–5889 (1995).
5. C. Galvan, P. G. Camoletto, F. Cristofani, P. P. Van Veldhoven, M. D. Ledesma, Anomalous surface distribution of glycosyl phosphatidyl inositol-anchored proteins in neurons lacking acid sphingomyelinase. *Mol. Biol. Cell* **19**, 509–522 (2008).
6. E. Gabandé-Rodríguez, P. Boya, V. Labrador, C. G. Dotti, M. D. Ledesma, High sphingomyelin levels induce lysosomal damage and autophagy dysfunction in Niemann Pick disease type A. *Cell Death Differ.* **21**, 864–875 (2014).
7. P. G. Camoletto, H. Vara, L. Morando, E. Connell, F. P. Marletto, M. Giustetto, M. Sassoè-Pognetto, P. P. van Veldhoven, M. D. Ledesma, Synaptic vesicle docking: Sphingosine regulates syntaxin1 interaction with Munc18. *PLOS ONE* **4**, e5310 (2009).
8. A. I. Arroyo, P. G. Camoletto, L. Morando, M. Sassoe-Pognetto, M. Giustetto, P. P. van Veldhoven, E. H. Schuchman, M. D. Ledesma, Pharmacological reversion of sphingomyelin-induced dendritic spine anomalies in a Niemann Pick disease type A mouse model. *EMBO Mol. Med.* **6**, 398–413 (2014).
9. A. Pérez-Cañamás, S. Benvegnù, C. B. Rueda, A. Rábano, J. Satrústegui, M. D. Ledesma, Sphingomyelin-induced inhibition of the plasma membrane calcium ATPase causes neurodegeneration in type A Niemann-Pick disease. *Mol. Psychiatry* **22**, 711–723 (2017).
10. K. Horinouchi, S. Erlich, D. P. Perl, K. Ferlinz, C. L. Bisgaier, K. Sandhoff, R. J. Desnick, C. L. Stewart, E. H. Schuchman, Acid sphingomyelinase deficient mice: A model of types A and B Niemann-Pick disease. *Nat. Genet.* **10**, 288–293 (1995).
11. K. Ferlinz, R. Hurwitz, G. Vielhaber, K. Suzuki, K. Sandhoff, Occurrence of two molecular forms of human acid sphingomyelinase. *Biochem. J.* **301** (Pt. 3), 855–862 (1994).
12. H. Grassmé, J. Bock, J. Kun, E. Gulbins, Clustering of CD40 ligand is required to form a functional contact with CD40. *J. Biol. Chem.* **277**, 30289–30299 (2002).
13. S. L. Schissel, G. A. Keesler, E. H. Schuchman, K. J. Williams, I. Tabas, The cellular trafficking and zinc dependence of secretory and lysosomal forms, two products of the acid sphingomyelinase gene. *J. Biol. Chem.* **273**, 18250–18259 (1998).
14. X. He, S. R. P. Miranda, X. Xiong, A. Dagan, S. Gatt, E. H. Schuchman, Characterization of human acid sphingomyelinase purified from the media of overexpressing Chinese hamster ovary cells. *Biochim. Biophys. Acta* **1432**, 251–264 (1999).
15. S. R. P. Miranda, X. He, C. M. Simonaro, S. Gatt, A. Dagan, R. J. Desnick, E. H. Schuchman, Infusion of recombinant human acid sphingomyelinase into Niemann-Pick disease mice leads to visceral, but not neurological, correction of the pathophysiology. *FASEB J.* **14**, 1988–1995 (2000).
16. M. P. Wasserstein, S. A. Jones, H. Soran, G. A. Diaz, N. Lippa, B. L. Thurberg, K. Culm-Merdek, E. Shamiyeh, H. Inguilizian, G. F. Cox, A. C. Puga, Successful within-patient dose escalation of olipudase alfa in acid sphingomyelinase deficiency. *Mol. Genet. Metab.* **116**, 88–97 (2015).
17. D. Graber, R. Salvayre, T. Levade, Accurate differentiation of neuronopathic and nonneuronopathic forms of Niemann-Pick disease by evaluation of the effective residual lysosomal sphingomyelinase activity in intact cells. *J. Neurochem.* **63**, 1060–1068 (1994).
18. J. C. Dodge, J. Clarke, C. M. Treleaven, T. V. Taksir, D. A. Griffiths, W. Yang, J. A. Fidler, M. A. Passini, K. P. Karey, E. H. Schuchman, S. H. Cheng, L. S. Shihabuddin, Intracerebroventricular infusion of acid sphingomyelinase corrects CNS manifestations in a mouse model of Niemann-Pick A disease. *Exp. Neurol.* **215**, 349–357 (2009).
19. R. J. Ziegler, E. A. Salegio, J. C. Dodge, J. Bringas, C. M. Treleaven, S. D. Bercury, T. J. Tamsett, L. Shihabuddin, P. Hadaczek, M. Fiandaca, K. Bankiewicz, R. K. Scheule, Distribution of acid sphingomyelinase in rodent and non-human primate brain after intracerebroventricular infusion. *Exp. Neurol.* **231**, 261–271 (2011).
20. M. Hocqemiller, L. Giersch, M. Audrain, S. Parker, N. Cartier, Adeno-associated virus-based gene therapy for CNS diseases. *Hum. Gene Ther.* **27**, 478–496 (2016).
21. S. R. P. Miranda, S. Erlich, V. L. Friedrich Jr., S. Gatt, E. H. Schuchman, Hematopoietic stem cell gene therapy leads to marked visceral organ improvements and a delayed onset of neurological abnormalities in the acid sphingomyelinase deficient mouse model of Niemann-Pick disease. *Gene Ther.* **7**, 1768–1776 (2000).
22. C. M. Barbon, R. J. Ziegler, C. Li, D. Armentano, M. Cherry, R. J. Desnick, E. H. Schuchman, S. H. Cheng, AAV8-mediated hepatic expression of acid sphingomyelinase corrects the metabolic defect in the visceral organs of a mouse model of Niemann-Pick disease. *Mol. Ther.* **12**, 431–440 (2005).
23. J. C. Dodge, J. Clarke, A. Song, J. Bu, W. Yang, T. V. Taksir, D. Griffiths, M. A. Zhao, E. H. Schuchman, S. H. Cheng, C. R. O'Riordan, L. S. Shihabuddin, M. A. Passini, G. R. Stewart, Gene transfer of human acid sphingomyelinase corrects neuropathology and motor deficits in a mouse model of Niemann-Pick type A disease. *Proc. Natl. Acad. Sci. U.S.A.* **102**, 17822–17827 (2005).
24. M. A. Passini, S. L. Macauley, M. R. Huff, T. V. Taksir, J. Bu, I.-H. Wu, P. A. Piepenhagen, J. C. Dodge, L. S. Shihabuddin, C. R. O'Riordan, E. H. Schuchman, G. R. Stewart, AAV vector-mediated correction of brain pathology in a mouse model of Niemann–Pick A disease. *Mol. Ther.* **11**, 754–762 (2005).
25. M. A. Passini, J. Bu, J. A. Fidler, R. J. Ziegler, J. W. Foley, J. C. Dodge, W. W. Yang, J. Clarke, T. V. Taksir, D. A. Griffiths, M. A. Zhao, C. R. O'Riordan, E. H. Schuchman, L. S. Shihabuddin,

Samaranch *et al.*, *Sci. Transl. Med.* **11**, eaat3738 (2019) 21 August 2019

14 of 15

S. H. Cheng, Combination brain and systemic injections of AAV provide maximal functional and survival benefits in the Niemann-Pick mouse. *Proc. Natl. Acad. Sci. U.S.A.* **104**, 9505–9510 (2007).

26. J. Bu, K. M. Ashe, J. Bringas, J. Marshall, J. C. Dodge, M. A. Cabrera-Salazar, J. Forsayeth, E. H. Schuchman, K. S. Bankiewicz, S. H. Cheng, L. S. Shihabuddin, M. A. Passini, Merits of combination cortical, subcortical, and cerebellar injections for the treatment of Niemann-Pick disease type A. *Mol. Ther.* **20**, 1893–1901 (2012).

27. E. A. Salegio, L. Samaranch, R. W. Jenkins, C. J. Clarke, C. Lamarre, J. Beyer, A. P. Kells, J. Bringas, W. San Sebastian, R. M. Richardson, K. H. Rosenbluth, Y. A. Hannun, K. S. Bankiewicz, J. Forsayeth, Safety study of adeno-associated virus serotype 2-mediated human acid sphingomyelinase expression in the nonhuman primate brain. *Hum. Gene Ther.* **23**, 891–902 (2012).

28. E. A. Salegio, A. P. Kells, R. M. Richardson, P. Hadaczek, J. Forsayeth, J. Bringas, S. P. Sardi, M. A. Passini, L. S. Shihabuddin, S. H. Cheng, M. S. Fiandaca, K. S. Bankiewicz, Magnetic resonance imaging-guided delivery of adeno-associated virus type 2 to the primate brain for the treatment of lysosomal storage disorders. *Hum. Gene Ther.* **21**, 1093–1103 (2010).

29. L. Samaranch, E. A. Salegio, W. San Sebastian, A. P. Kells, K. D. Foust, J. R. Bringas, C. Lamarre, J. Forsayeth, B. K. Kaspar, K. S. Bankiewicz, Adeno-associated virus serotype 9 transduction in the central nervous system of nonhuman primates. *Hum. Gene Ther.* **23**, 382–389 (2012).

30. K. D. Foust, E. Nurre, C. L. Montgomery, A. Hernandez, C. M. Chan, B. K. Kaspar, Intravascular AAV9 preferentially targets neonatal neurons and adult astrocytes. *Nat. Biotechnol.* **27**, 59–65 (2009).

31. S. J. Gray, V. Matagne, L. Bachaboina, S. Yadav, S. R. Ojeda, R. J. Samulski, Preclinical differences of intravascular AAV9 delivery to neurons and glia: A comparative study of adult mice and nonhuman primates. *Mol. Ther.* **19**, 1058–1069 (2011).

32. L. Samaranch, W. S. Sebastian, A. P. Kells, E. A. Salegio, G. Heller, J. R. Bringas, P. Pivirotto, S. DeArmond, J. Forsayeth, K. S. Bankiewicz, AAV9-mediated expression of a non-self protein in nonhuman primate central nervous system triggers widespread neuroinflammation driven by antigen-presenting cell transduction. *Mol. Ther.* **22**, 329–337 (2014).

33. L. Samaranch, E. A. Salegio, W. San Sebastian, A. P. Kells, J. R. Bringas, J. Forsayeth, K. S. Bankiewicz, Strong cortical and spinal cord transduction after AAV7 and AAV9 delivery into the cerebrospinal fluid of nonhuman primates. *Hum. Gen. Ther.* **24**, 526–532 (2013).

34. L. M. Sanftner, B. M. Suzuki, M. M. Doroudchi, L. Feng, A. McClelland, J. R. Forsayeth, J. Cunningham, Striatal delivery of rAAV-hAADC to rats with preexisting immunity to AAV. *Mol. Ther.* **9**, 403–409 (2004).

35. M. D. Ledesma, A. Prinetti, S. Sonnino, E. H. Schuchman, Brain pathology in Niemann Pick disease type A: Insights from the acid sphingomyelinase knockout mice. *J. Neurochem.* **116**, 779–788 (2011).

36. S. L. Macauley, R. L. Sidman, E. H. Schuchman, T. Taksir, G. R. Stewart, Neuropathology of the acid sphingomyelinase knockout mouse model of Niemann-Pick A disease including structure-function studies associated with cerebellar Purkinje cell degeneration. *Exp. Neurol.* **214**, 181–192 (2008).

37. R. Testi, Sphingomyelin breakdown and cell fate. *Trends Biochem. Sci.* **21**, 468–471 (1996).

38. V. Teichgräber, M. Ulrich, N. Endlich, J. Riethmüller, B. Wilker, C. C. De Oliveira-Munding, A. M. van Heeckeren, M. L. Barr, G. von Kürthy, K. W. Schmid, M. Weller, B. Tümmler, F. Lang, H. Grassme, G. Döring, E. Gulbins, Ceramide accumulation mediates inflammation, cell death and infection susceptibility in cystic fibrosis. *Nat. Med.* **14**, 382–391 (2008).

39. N. Hagen, P. P. van Veldhoven, R. L. Proia, H. Park, A. H. Merrill Jr., G. van Echten-Deckert, Subcellular origin of sphingosine 1-phosphate is essential for its toxic effect in lyase-deficient neurons. *J. Biol. Chem.* **284**, 11346–11353 (2009).

40. E. Lloyd-Evans, A. J. Morgan, X. He, D. A. Smith, E. Elliot-Smith, D. J. Sillence, G. C. Churchill, E. H. Schuchman, A. Galione, F. M. Platt, Niemann-Pick disease type C1 is a sphingosine storage disease that causes deregulation of lysosomal calcium. *Nat. Med.* **14**, 1247–1255 (2008).

41. J. Naidoo, M. Stanek, K. Ohno, S. Trewman, L. Samaranch, P. Hadaczek, C. O'Riordan, J. Sullivan, W. San Sebastian, J. R. Bringas, C. Snieckus, A. Mahmoodi, A. Mahmoodi, J. Forsayeth, K. S. Bankiewicz, L. S. Shihabuddin, Extensive transduction and enhanced spread of a modified AAV2 capsid in the non-human primate CNS. *Mol. Ther.* **26**, 2418–2430 (2018).

42. V. Sudhakar, A. Mahmoodi, J. R. Bringas, J. Naidoo, A. Kells, L. Samaranch, M. S. Fiandaca, K. S. Bankiewicz, Development of a novel frameless skull-mounted ball-joint guide array for use in image guided neurosurgery. *J. Neurosurg.* **15**, 1–10 (2019).

43. K. Ohno, L. Samaranch, P. Hadaczek, J. R. Bringas, P. C. Allen, V. Sudhakar, D. E. Stockinger, C. Snieckus, M. V. Campagna, W. San Sebastian, J. Naidoo, H. Chen, J. Forsayeth, E. A. Salegio, G. G. C. Hwa, K. S. Bankiewicz, Kinetics and MR-based monitoring of AAV9 vector delivery into cerebrospinal fluid of nonhuman primates. *Mol. Ther. Methods Clin. Dev.* **13**, 47–54 (2019).

44. G. Liu, I. Martins, J. A. Wemmie, J. A. Chiorini, B. L. Davidson, Functional correction of CNS phenotypes in a lysosomal storage disease model using adeno-associated virus type 4 vectors. *J. Neurosci.* **25**, 9321–9327 (2005).

45. M. L. Katz, L. Tecedor, Y. Chen, B. G. Williamson, E. Lysenko, F. A. Wininger, W. M. Young, G. C. Johnson, R. E. H. Whiting, J. R. Coates, B. L. Davidson, AAV gene transfer delays disease onset in a TPP1-deficient canine model of the late infantile form of Batten disease. *Sci. Transl. Med.* **7**, 313ra180 (2015).

46. A. Bacyinski, M. Xu, W. Wang, J. Hu, The paravascular pathway for brain waste clearance: Current understanding, significance and controversy. *Front. Neuroanat.* **11**, 101 (2017).

47. R. H. Smith, J. R. Levy, R. M. Kotin, A simplified baculovirus-AAV expression vector system coupled with one-step affinity purification yields high-titer rAAV stocks from insect cells. *Mol. Ther.* **17**, 1888–1896 (2009).

48. G. P. Cognato, P. M. Agostinho, J. Hockemeyer, C. E. Müller, D. O. Souza, R. A. Cunha, Caffeine and an adenosine A$_{2A}$ receptor antagonist prevent memory impairment and synaptotoxicity in adult rats triggered by a convulsive episode in early life. *J. Neurochem.* **112**, 453–462 (2010).

49. M. R. Hojjati, X.-C. Jiang, Rapid, specific, and sensitive measurements of plasma sphingomyelin and phosphatidylcholine. *J. Lipid Res.* **47**, 673–676 (2006).

50. X. He, F. Chen, A. Dagan, S. Gatt, E. H. Schuchman, A fluorescence-based, high-performance liquid chromatographic assay to determine acid sphingomyelinase activity and diagnose types A and B Niemann–Pick disease. *Anal. Biochem.* **314**, 116–120 (2003).

51. S. L. Eaton, S. Cumyn, D. King, R. A. Kline, S. M. Carpanini, J. del-Pozo, R. Barron, T. M. Wishart, Quantitative imaging of tissue sections using infrared scanning technology. *J. Anat.* **228**, 203–213 (2016).

Science Translational Medicine

Adeno-associated viral vector serotype 9–based gene therapy for Niemann-Pick disease type A

Lluis Samaranch, Azucena Pérez-Cañamás, Beatriz Soto-Huelin, Vivek Sudhakar, Jerónimo Jurado-Arjona, Piotr Hadaczek, Jesús Ávila, John R. Bringas, Josefina Casas, Haifeng Chen, Xingxuan He, Edward H. Schuchman, Seng H. Cheng, John Forsayeth, Krystof S. Bankiewicz and María Dolores Ledesma

Safe and effective gene delivery

Niemann-Pick type A disease (NPD-A) is caused by loss-of-function mutations in the gene encoding for acid sphingomyelinase (ASM). Patients present mental retardation with prominent loss of early motor skills and cognitive decline and early death. Gene replacement therapy has been shown to be effective in other monogenic neurological disorders. Now, Samaranch *et al.* evaluated the safety and efficacy of adeno-associated viral vector serotype 9 (AAV9)–based gene therapy. AAV9-mediated delivery of human ASM in the cerebellomedullary cistern allowed widespread gene expression in the brain and spinal cord of nonhuman primates without signs of toxicity. The treatment prevented motor and memory impairment and increased survival in a mouse model of NPD-A.